

Function-on-Scalar Quantile Regression with Application to Mass Spectrometry Proteomics Data

Yusha Liu^{*}, Meng Li^{*} and Jeffrey S. Morris[†]

^{*}*Department of Statistics, Rice University*

[†]*Department of Biostatistics, University of Texas MD Anderson Cancer Center*

December 15, 2024

Abstract

Mass spectrometry proteomics, characterized by spiky, spatially heterogeneous functional data, can be used to identify potential cancer biomarkers. Existing mass spectrometry analyses utilize mean regression to detect spectral regions that are differentially expressed across groups. However, given the inter-patient heterogeneity that is a key hallmark of cancer, many biomarkers are only present at aberrant levels for a subset of, not all, cancer samples. Differences in these biomarkers can easily be missed by mean regression, but might be more easily detected by quantile-based approaches. Thus, we propose a unified Bayesian framework to perform quantile regression on functional responses. Our approach utilizes an asymmetric Laplace working likelihood, represents the functional coefficients with basis representations which enable borrowing of strength from nearby locations, and places a global-local shrinkage prior on the basis coefficients to achieve adaptive regularization. Different types of basis transform and continuous shrinkage priors can be used in our framework. An efficient Gibbs sampler is developed to generate posterior samples that can be used to perform Bayesian estimation and inference while accounting for multiple testing. Our framework performs quantile regression and coefficient regularization in a unified manner, allowing them to inform each other and leading to improvement in performance over competing methods as demonstrated by simulation studies. We apply this model to identify proteomic biomarkers of pancreatic cancer missed by previous mean-regression based approaches. Supplementary materials for this article are available online.

Keywords: Functional data analysis, Functional response regression, Quantile regression, Bayesian hierarchical model, Global-local shrinkage, Proteomic biomarker

1 Introduction

1.1 Mass Spectrometry Proteomics

The rapid advancement of molecular biotechnology has led to the ability to make large-scale molecular measurements using high-throughput technologies at various molecular resolution levels, including DNA, mRNA, epigenetic, metabolite, and protein levels. DNA and mRNA have been most frequently studied, largely because nucleotide sequences are easier to study and analyze in nature than proteins and metabolites. However, it is proteins, rather than DNA or messenger RNA, that play a fundamental functional role in the molecular processes underlying various diseases including cancer. As a result, there is great interest in studying proteins directly and identifying proteomic biomarkers of cancer that can potentially be used for early detection, new drug target identification and precision medicine strategies.

Mass spectrometry is an analytical technique to survey a large number of different proteins, peptides, or metabolites in a biological sample by first ionizing the particles from the sample, then separating the ions based on their mass-to-charge ratio, and detecting the ions and assembling them into a mass spectrum for each sample. Commonly used ionization techniques for solid and liquid biological samples include MALDI (matrix assisted laser desorption and ionization) and ESI (electrospray ionization), and popular mass analyzers which separate charged particles include TOF (time-of-flight) analyzer and quadrupole mass analyzers. Regardless of the ionization and separation techniques used, the resulting mass spectrum is a highly spiky and irregular function with many peaks, with the spectral intensity $y(t)$ approximating the relative abundance of a protein or peptide with the mass-to-charge ratio of t in the given biological sample. To further enhance its capability for protein identification and quantification, mass spectrometry is often used in tandem with liquid chromatography, which first separates the proteomic sample through an LC column over a series of elution times based on hydrophobicity or other physical properties before the mass spectrometry procedure, resulting in 2D mass spectrometry data (LC-MS) with one dimension representing elution time and the other dimension representing the mass-to-charge ratio ([Zhang et al., 2009](#); [Liao et al., 2014](#)).

1.2 Interpatient Heterogeneity and Pancreatic Cancer Proteomic Markers

At the University of Texas M.D. Anderson Cancer Center, a study was conducted using MALDI-TOF to discover potential proteomic markers of pancreatic cancer. The left column of Figure 1 displays the raw spectrum of a pancreatic cancer patient and a normal control from this dataset, which demonstrates the highly spiky and irregular nature of mass spectrometry data. In this study, researchers collected the blood serum samples from 139 pancreatic cancer patients and 117 normal controls and ran them on a MALDI-TOF mass spectrometer to produce a mass spectrum for each sample (Koomen et al., 2005; Morris et al., 2008). The primary goal is to identify proteins, represented by spectral regions, with differential abundance between pancreatic cancer and normal samples, and potentially useful as diagnostic, prognostic, or predictive biomarkers.

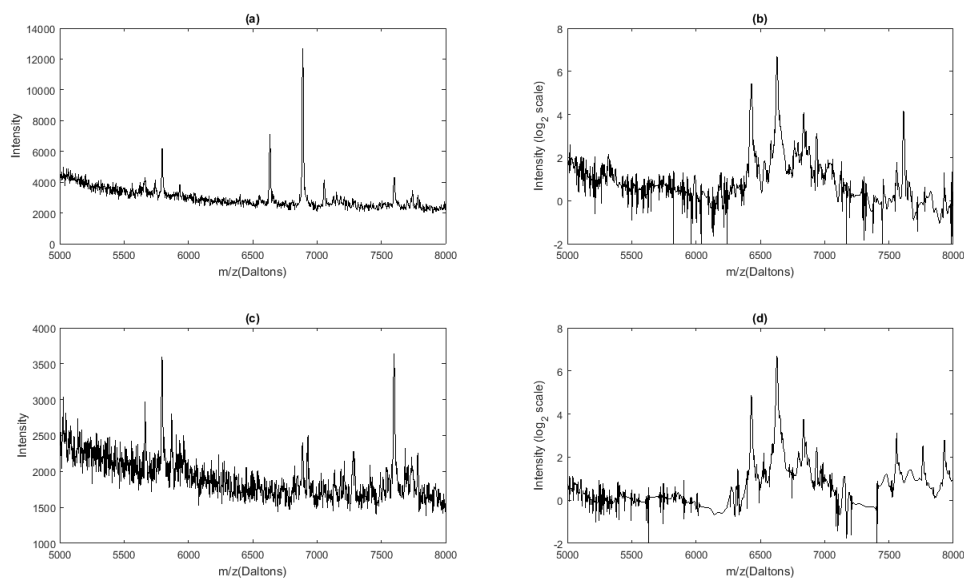


Figure 1: *Sample spectra from the pancreatic cancer dataset.* The first column shows the raw spectrum of a normal control (a) and a cancer patient (c) randomly chosen from the pancreatic cancer MALDI-TOF mass spectrometry dataset. The second column displays the corresponding spectra of the normal control (b) and the cancer patient (d) after preprocessing, which includes baseline correction, normalization, denoising and \log_2 transformation.

Classic approaches to analyzing mass spectrometry data depend on first performing peak detection, and then only analyzing the detected locations and sometimes intensities of those

peaks. For example, after applying a feature detection method to identify m peaks for each of N spectra, these can be put together into an $N \times m$ matrix and analyzed to find which of the m features are associated with factors of interest (cancer/normal). While this two-step approach seems intuitive and reasonable, important proteomic differences across factors of interest might be missed if the feature detection procedure in the first step fails to detect peaks corresponding to the corresponding protein. An alternative to this feature extraction-based approach is to model the entire mass spectra as functional data using functional data analysis techniques. [Morris \(2012\)](#) applied the wavelet-based functional mixed model introduced by [Morris and Carroll \(2006\)](#) to this pancreatic cancer dataset to identify differentially expressed regions between cancer and control in the range from $t = 4,000$ to $t = 20,000$ Daltons, and flagged approximately 50% more significant spectral regions than the more commonly used peak detection approach, suggesting that the functional modeling approach can yield greater power for biomarker discovery.

As is the case for nearly all mass spectrometry analyses, both of these feature extraction and functional data approaches utilize mean regression, in which the mean expression levels are compared across pre-defined groups. However, given the interpatient heterogeneity that is a hallmark of cancer, for many potentially useful proteomic biomarkers only a subset of cancer patients may have protein levels that differ from the normal controls. These may be difficult to detect using statistical methods focused on the mean, and might be more easily detected by quantile-based methods. In those cases, we may have more power to find cancer-normal differences when looking in the tails of the distributions rather than the mean.

To explore this possibility, we computed the difference in the mean and sample quantiles between the cancer and normal groups for each spectral position between 5000D and 8000D in [Figure 2 \(a\)](#). Note that in the region (5700D, 6000D), there appear to be huge differences in the 90th percentile in the upper tail, while there is little evidence of a difference in the median or mean. More closely inspecting one location at 5764.1D, [Figure 2 \(b\)](#) and [\(c\)](#) show a strongly right skewed pattern of the spectral intensity distribution for the cancer cohort and a slightly left skewed distribution with a similar mode for the normal cohort. This observation suggests that a small subset of pancreatic cancer patients have much higher protein levels than other patients and healthy controls at 5764.1D, but mean or median regression might not be able to detect this important pattern. While these plots are suggestive of some difference, formal statistical methods are needed to assess these potential differences, and these methods need to account for the multiple testing problem inherent to these high-dimensional data. Our goal in this paper is to develop such methods.

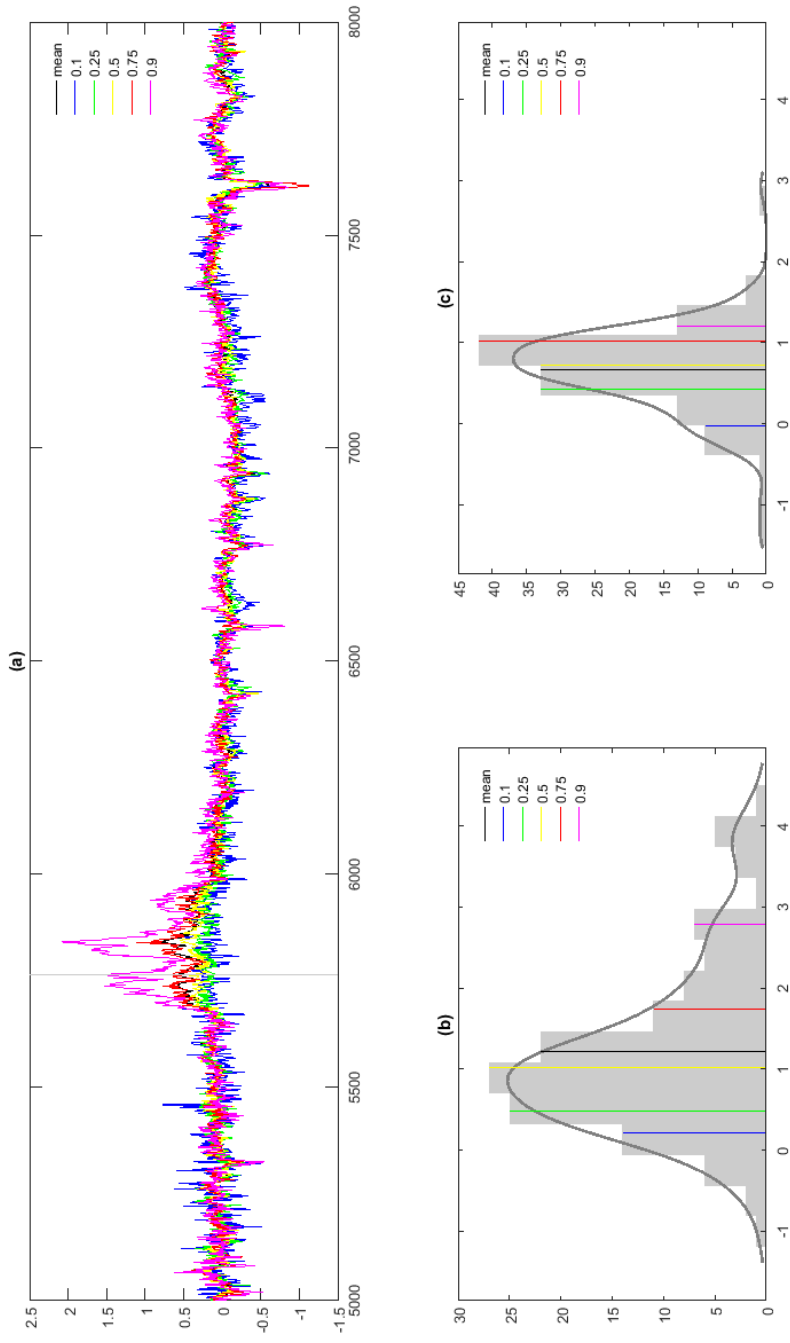


Figure 2: *Empirical estimates of the cancer main effect for multiple quantile levels and mean.* (a) shows the differences of the sample mean and multiple quantiles in the spectral region [5000D, 8000D] between the cancer and normal cohorts from the preprocessed pancreatic cancer dataset. The vertical line represents the spectral location 5764.1D, where we observe a huge difference between the two groups in the 90th sample quantiles. The histograms of the spectral intensities at 5764.1D are shown respectively for the cancer cohort (b) and the normal cohort (c), with the sample mean and quantiles marked by vertical lines.

1.3 Literature review: Quantile Regression and Functional Quantile Regression

Quantile regression, first introduced by [Koenker and Bassett Jr \(1978\)](#), has been widely used in many application areas to study the effect of predictor variables on a given quantile level of the response, and can reveal important information about how the entire distribution of response varies with predictors in ways that might not be captured by mean regression. Traditionally, quantile regression is formulated as an optimization problem in which the regression coefficients are estimated by minimizing the check loss function ([Koenker, 2005](#)).

Recently, Bayesian quantile regression has gained a lot of attention, partly because posterior samples drawn from Markov Chain Monte Carlo procedure can be used to perform Bayesian inference on any model parameter in a straightforward manner. A great variety of likelihoods have been proposed to perform Bayesian quantile regression; see [Lum et al. \(2012\)](#) and [Yang et al. \(2016\)](#) for a comprehensive overview. Among them, asymmetric Laplace (AL) error distribution ([Yu and Moyeed, 2001](#)) is widely adopted in conditional quantile regression models, based on the fact that the maximization of an AL likelihood is equivalent to the minimization of the check loss function.

In the present context, we would like to perform quantile regression for each spectral location, which is a generalization consisting of quantile regression of functional responses on scalar predictors that we henceforth refer to as *functional quantile regression*(FQR). An approach has recently been proposed to model the effect of scalar predictors on the conditional quantile of a scalar response nonparametrically under additive modeling framework ([Fasiolo et al., 2018](#)). There has also been recent work on scalar-on-function quantile regression where the conditional quantile of a scalar response is modeled as an inner product of a functional predictor and an unknown coefficient function ([Cardot et al., 2005](#); [Ferraty et al., 2005](#); [Chen and Müller, 2012](#); [Kato, 2012](#); [Li et al., 2016](#)). However, to our knowledge, very few statistical methods have been developed to perform FQR, i.e., function-on-scalar quantile regression. One approach would be to simply fit independent quantile regressions for each t , which is unbiased but expected to be inefficient since it does not borrow strength from nearby t as is typical in functional data modeling approaches. As emphasized in a review of functional regression techniques in [Morris \(2015\)](#), most functional regression methods borrow strength across t by using basis functions and penalization to induce smoothness and regularization in the functional coefficients. The functional linear array model proposed by [Brockhaus et al. \(2015\)](#) is a general framework for functional regression which could be used to perform FQR if

the check loss function is chosen. However, as we show, this framework’s utilization of spline basis functions and global L2 penalization may not work well for complex, irregular functions like the mass spectrometry data here, and the FDboost fitting approach (Brockhaus and Ruegamer, 2017) has scalability problems in this setting. New methods for performing functional response quantile regression are needed for data like these.

In this paper, we present a new unified Bayesian FQR framework that performs quantile regression across all t by adopting an AL likelihood and adaptively regularizing the functional regression coefficients using a basis representation with shrinkage priors on the corresponding basis coefficients. Our framework is highly general in that any basis functions and computationally tractable shrinkage priors can be chosen, depending on the characteristics of the functional data to be analyzed. We develop an efficient Gibbs sampler to fit this fully Bayesian hierarchical model in an automated fashion with no tuning required, which yields posterior samples that can be used to perform Bayesian inference on the regression coefficients that adjusts for multiple testing over t . Our approach is computationally efficient and can handle functional data observed on grids of hundreds to thousands.

The rest of this paper is organized as follows. We introduce the Bayesian functional quantile regression framework in Section 2.1, describe the procedures for posterior computation of our proposed model in Section 2.2, and discuss posterior inference in Section 2.3. We conduct simulation studies to assess the performance of our proposed model and compare to other alternatives in Section 3, apply our model to the motivating pancreatic cancer mass spectrometry dataset and discuss the findings in Section 4, and conclude the paper with a discussion in Section 5.

2 Methods

2.1 Bayesian functional quantile regression (FQR) model

Suppose a sample of N curves $\mathbf{Y}(t) = (Y_1(t), \dots, Y_N(t))'$ are observed on the same compact set \mathcal{T} , and \mathbf{X} is the $N \times p$ design matrix. For the τ th quantile, the model we use to perform Bayesian functional quantile regression is given by

$$\mathbf{Y}(t) = \mathbf{X}\mathbf{B}^\tau(t) + \mathbf{E}^\tau(t), \tag{1}$$

where $\mathbf{B}^\tau(t) = (B_1^\tau(t), \dots, B_p^\tau(t))'$ is a vector of regression coefficient functions measuring the effect of covariates \mathbf{X} on the τ th quantile of response function Y at position t , and

$\mathbf{E}^\tau(t) = (E_1^\tau(t), \dots, E_N^\tau(t))'$ is a vector of residual error functions that follow asymmetric Laplace distribution $\text{AL}(0, \tau, \sigma(t))$ at position t , independently across positions and samples.

The probability density function of $\text{AL}(0, \tau, \sigma(t))$ is given by

$$f(\epsilon|\mu, \tau, \sigma) = \frac{\tau(1-\tau)}{\sigma} \exp\left[-\frac{\rho_\tau(\epsilon - \mu)}{\sigma}\right],$$

where $\rho_\tau(u) = u(\tau - \mathbb{1}_{(u \leq 0)})$ is the check loss function. The τ th quantile of the asymmetric Laplace distribution $\text{AL}(0, \tau, \sigma(t))$ is zero, therefore, model (1) implies $Q_\tau(\mathbf{Y}(t)|\mathbf{X}) = \mathbf{X}\mathbf{B}^\tau(t)$ for $\forall t \in \mathcal{T}$, with $Q_\tau(\mathbf{Y}(t)|\mathbf{X})$ denoting the τ th quantile of $\mathbf{Y}(t)$ conditional on \mathbf{X} , and $B_a^\tau(t)$ representing the partial effect of the covariate a on the τ th quantile of $\mathbf{Y}(t)$. An asymmetric Laplace random variable ϵ can be represented as a scale mixture of normal distributions (Reed and Yu, 2009), i.e.,

$$\epsilon \stackrel{d}{=} \frac{1-2\tau}{\tau(1-\tau)}\xi + \sqrt{\frac{2\sigma\xi}{\tau(1-\tau)}}Z,$$

where Z is a standard normal random variable and ξ is an independent exponential random variable with mean σ . This representation allows the development of an efficient partially collapsed Gibbs sampler for Bayesian quantile regression as detailed in Section 2.2.

To simplify notation, henceforth we omit the quantile level τ in the hierarchical modeling assumptions we make for the functional quantile regression coefficients $\mathbf{B}^\tau(t)$, with the understanding that the coefficients correspond to a particular choice of quantile τ .

Basis Representation and Shrinkage Priors: As is typical for functional regression methods, we will induce regularization in the functional coefficients $B_a(t)$ using a basis representation and penalization induced by sparsity priors. For a given chosen finite basis representation $\{\phi_k(t), k = 1, \dots, K\}$, we specify a basis representation for $B_a(t)$,

$$B_a(t) = \sum_{k=1}^K B_{ak}^* \phi_k(t). \tag{2}$$

Common choices of the basis functions include splines, functional principal components, Fourier bases and wavelets.

We induce regularization of $B_a(t)$ by penalizing the basis coefficients B_{ak}^* using an appropriate global-local shrinkage prior (Polson and Scott, 2010). For extra flexibility in regularization, we group the basis functions $k = 1, \dots, K$ into regularization subsets $j = 1, \dots, J$, each containing H_j basis functions such that $K = \sum_{j=1}^J H_j$. This allows different sets of basis functions to experience different levels of shrinkage, which can lead to more adaptive regularization of $B_a(t)$. For example, for wavelet bases, j can index the wavelet scale, allowing

higher and lower frequency wavelets to experience different levels of shrinkage. For functional principal components analysis, the H_j eigenfunctions that share the same $\lfloor \log_{10}(\eta_k) \rfloor$, where η_k denotes the corresponding eigenvalue, can be grouped into the same regularization subset j , allowing the possibility that dimensions explaining a higher proportion of the functional variability may also be more important for representing the functional predictor $B_a(t)$, as well, and be allowed to experience less shrinkage.

Given the regularization groups, a general global-local prior can be expressed as

$$B_{ajh}^* \sim N(0, \lambda_{ajh}^2 \psi_{aj}^2), \quad \lambda_{ajh} \sim g_1, \quad \psi_{aj} \sim g_2(\Theta_{aj}). \quad (3)$$

This prior is comprised of a scale mixture of Gaussians, with a global shrinkage parameter ψ_{aj}^2 and local shrinkage parameter λ_{ajh}^2 . The local shrinkage parameters λ_{ajh} are assigned some prior g_1 , allowing different amount of shrinkage on B_{ajh}^* within the regularization subset j . The global shrinkage parameter ψ_{aj} controls the overall level of shrinkage in the subset j , and is assigned a prior g_2 indexed by the hyperparameter Θ_{aj} .

Conditioning on ψ_{aj} and integrating out λ_{ajh} , different choices of g_1 result in different marginal distributional forms that lead to different types of penalization and forms of regularization. A degenerate distribution $\lambda_{ajh} \sim \delta_1$ induces a Gaussian prior on B_{ajh}^* , leading to L2 penalization which would be a natural choice of regularization if spline basis functions are used. $\lambda_{ajh}^2 \sim \text{Exp}(\frac{1}{2})$ induces a Laplace prior on B_{ajh}^* , leading to L1 penalization and for which the maximum *a posteriori* estimator is equivalent to the lasso estimate widely used for variable selection. $\lambda_{ajh} \sim C^+(0, 1)$ induces a horseshoe prior (Carvalho et al., 2009, 2010) on B_{ajh}^* , leading to non-linear adaptive shrinkage particularly desirable for wavelet transform, which tends to concentrate the signals in the data space on a relatively small number of wavelet coefficients that are usually large in magnitude, with the remaining coefficients being small and mostly consisting of noise. The infinitely tall spike of the horseshoe prior at the origin can strongly shrink the small coefficients, and its symmetric flat and Cauchy-like tails can avoid over-shrinkage of the large coefficients and retain the dominant local features in the observed data (Carvalho et al., 2009).

To summarize, our proposed model performs quantile regression on functional responses based on model (1), represents the coefficient functions using an appropriate basis representation as specified by model (2), and regularizes the basis coefficients by employing a global-shrinkage prior in model (3). Henceforth, we term this model as Bayesian functional quantile regression (FQR).

In practice, the functional responses are observed only on some discrete grid. Because our model is built for functional data sampled on a sufficiently dense grid, interpolation can be reasonably used to get a common grid for functional observations across subjects. If we assume that $\mathbf{Y}(t) = (Y_1(t), \dots, Y_N(t))'$ are all observed on a common grid $\mathbf{t} = (t_1, \dots, t_T)'$, and utilize the scale mixture representation of AL, we can represent the discrete version of model (1) as

$$Y_i(t_l) = \mathbf{X}'_i \mathbf{B}^\tau(t_l) + \frac{1 - 2\tau}{\tau(1 - \tau)} \xi_i(t_l) + \sqrt{\frac{2\xi_i(t_l)\sigma(t_l)}{\tau(1 - \tau)}} Z_i(t_l), \quad (4)$$

for sample $i = 1, \dots, N$ and position $l = 1, \dots, T$. In model (4), \mathbf{Y} is an $N \times T$ matrix of functional responses with $Y_i(t_l)$ being the observation for sample i at position l , \mathbf{B} is a $p \times T$ matrix of functional coefficients with its l^{th} column $\mathbf{B}^\tau(t_l) = (B_1^\tau(t_l), \dots, B_p^\tau(t_l))'$ being the vector of quantile regression coefficients at position l , $\sigma(t_l)$ is the scale parameter of the AL distribution at position l , $\xi_i(t_l)$ is the latent variable for sample i at position l following exponential distribution with mean $\sigma(t_l)$ independently across positions and samples, and $Z_i(t_l)$ is a standard normal variable *i.i.d* across positions and samples.

Equation (2) can now be expressed as

$$\mathbf{B} = \mathbf{B}^* \Phi, \quad (5)$$

where \mathbf{B}^* is a $p \times K$ matrix of basis coefficients, Φ is a full rank $K \times T$ matrix whose k th row corresponds to the basis function ϕ_k evaluated on the discrete grid \mathbf{t} .

2.2 Posterior computation

We take a fully Bayesian approach to fit the FQR model. For appropriately chosen priors g_1 and g_2 , posterior sampling proceeds via an efficient blocked Gibbs sampler with data augmentation if necessary. We outline the steps to draw posterior samples of the parameters in model (4) as follows, and leave the full computational details in the supplementary materials.

1. For each l , sample $(\sigma(t_l) | \mathbf{B}(t_l), \mathbf{y}(t_l))$ from an inverse Gamma distribution;
2. For each i and l , sample $(1/\xi_i(t_l) | \mathbf{B}(t_l), \sigma(t_l), \mathbf{y}(t_l))$ from an inverse Gaussian distribution;
3. For each a , sample $(\mathbf{B}_a^* | \mathbf{B}_{-a}^*, \boldsymbol{\lambda}_a, \boldsymbol{\psi}_a, \boldsymbol{\xi}, \boldsymbol{\sigma}, \mathbf{Y})$ from multivariate normal;

4. For each a, j, h , sample the local shrinkage parameter $(\lambda_{ajh}|B_{ajh}^*, \psi_{aj})$; for each a, j , sample the global shrinkage parameter $(\psi_{aj}|\lambda_{aj}, \mathbf{B}_{aj}^*)$;
5. Project the rows of the updated basis coefficients \mathbf{B}^* back to the data space using equation (5).

2.3 Posterior inference

The posterior samples obtained from the MCMC procedure can be used to construct a Bayesian estimator and perform Bayesian inference for any function of the parameters in model (4). In particular, for the functional coefficient $\mathbf{B}_a = (B_a(t_1), \dots, B_a(t_L))'$, a $100(1 - \alpha)\%$ simultaneous credible band can be constructed from the posterior samples of \mathbf{B}_a using the method described by [Ruppert et al. \(2003\)](#) for $\alpha \in (0, 1)$. Suppose $\{\mathbf{B}_a^{(g)}, g = 1, \dots, G\}$ are the G posterior samples of \mathbf{B}_a , where $\mathbf{B}_a^{(g)} = (B_a^{(g)}(t_1), \dots, B_a^{(g)}(t_T))'$. Let $m(B_a(t_l))$ and $\hat{sd}(B_a(t_l))$ denote the mean and standard deviation of $B_a(t_l)$ estimated from the G posterior samples, a $100(1 - \alpha)\%$ simultaneous credible band can be constructed by

$$\left[m(B_a(t_l)) - q_\alpha \hat{sd}(B_a(t_l)), m(B_a(t_l)) + q_\alpha \hat{sd}(B_a(t_l)) \right], \quad l = 1, \dots, T,$$

where q_α is the $(1 - \alpha)$ sample quantile of

$$\max_{1 \leq l \leq T} \left| \frac{B_a^{(g)}(t_l) - m(B_a(t_l))}{\hat{sd}(B_a(t_l))} \right|, \quad g = 1, \dots, G.$$

Given a quantile level τ and covariate a , it is often of interest to identify the locations t for which $B_a(t)$ is significantly different from zero while adjusting for multiple testing in the functional data context. For example, in the pancreatic cancer mass spectrometry dataset, if the covariate a denotes cancer status, then the identified locations t would correspond to the spectral regions for which the τ th quantile of protein expressions significantly differs between the cancer and normal populations. In this paper, we consider an approach that performs functional inference based on simultaneous band scores, or *SimBaS* ([Meyer et al., 2015](#)), which involve inverting the joint credible bands for each t . SimBaS of a functional location t_l is defined as the minimum α for which the $100(1 - \alpha)\%$ simultaneous credible band excludes zero at t_l . At a pre-chosen level α , we flag t_l as significant if its SimBaS is less than or equal to α . Given that it is based on the $100(1 - \alpha)\%$ simultaneous credible band for which there is a $100(1 - \alpha)\%$ posterior probability that the *entire* function $B_a(t)$ lies within the corresponding band, use of this measure effectively adjusts for multiple testing based on an experimentwise error rate criterion.

In terms of flagging significant spectral regions, the SimBaS account for statistical significance, but not practical significance. One may wish to also require a difference of some minimum effect size to flag a spectral region as significant, which can be specified as a minimum fold change δ if the log spectral intensities are measured. In that case, one may require $\text{SimBaS} < \alpha$ and $|B_a(t)| \geq \log_2 \delta$, requiring at least a δ -fold change for the τ th quantile of protein expressions between cancer and normal groups, quantified by posterior mean estimates of $B_a(t)$. To consider a region as significant, we also require at least 3 consecutive locations to be flagged based on the SimBaS and effect size.

3 Simulation studies

We conducted simulation studies to evaluate the performance of our proposed model and compare to several straightforward approaches that some might use in the FQR setting.

Simulation design: The shapes of mass spectrometry peaks can be approximated by Gaussian densities (Zhang et al., 2009), with the heights of the peaks roughly quantifying the relative abundance of proteins at the corresponding spectral locations. Thus, in constructing a simulation to mimic mass spectrometry data, we utilize peaks with Gaussian shapes. While the peak shapes were chosen to be Gaussian, the distributions of peak intensities across samples were not. Instead, they were chosen to have skewed or heavy tailed distributions to mimic the distributions we see in the real protein data. For some peaks, we simulate the data such that there is no difference in peak intensity between cancer and normal groups and for others, we simulate them to have identical peak shape but different intensity distributions. These distributions were constructed to have identical means (if they exist) but either different degrees of skewness or tail heaviness so that there would be a difference in the distributional tails but not in the means.

Specifically, we considered two different settings for the distribution of peak magnitudes across subjects, which we refer to as (i) symmetric heavy tailed setting and (ii) right skewed setting, respectively. For one simulated dataset from each setting, functional data were generated for two groups based on the following model, with 200 curves per group

$$\mathbf{y}_a(t) = \sum_{k=1}^7 c_{k,a} f(t | \mu_k, \sigma_k) + \mathbf{e}(t),$$

where $a(= 1, 2)$ denotes the group status, $f(t | \mu_k, \sigma_k)$ is the probability density function of a normal distribution with mean μ_k and standard deviation σ_k , which corresponds to a

Gaussian shaped peak in $\mathbf{y}_a(t)$ centered at μ_k , and $c_{k,a}$ is a random variable that dictates the magnitudes of this peak across subjects in group a . $\mathbf{e}(t)$ is a Gaussian AR(1) process with lag 1 autocorrelation $\rho = 0.8$ and a marginal distribution $e(t) \sim N(0, 9)$. The functional response $\mathbf{y}_a(t)$ is observed on an equally spaced grid of 501 on the interval $[0, 15]$. The distributions of $c_{k,a}$ and the values taken by μ_k and σ_k are provided in Table 1. We simulated 100 replicate datasets for each setting.

Table 1: *Parameter specifications of the data generating models in simulations.*

Basis index	Both settings		Setting (i)		Setting (ii)	
	μ_k	σ_k	$c_{k,1}$	$c_{k,2}$	$c_{k,1}$	$c_{k,2}$
1	1.209	0.145	$N(30, 1.5^2)$	$N(30, 1.5^2)$	$N(30, 1.5^2)$	$N(30, 1.5^2)$
2	2.938	0.150	$N(30, 1.5^2)$	$N(30, 1.5^2)$	$IG(1, 0.35) + 30$	$N(30.6, 0.4^2)$
3	4.700	0.155	$1.75t_2 + 30$	$N(30, 1^2)$	$N(30, 1.5^2)$	$N(30, 1.5^2)$
4	7.267	0.160	$N(30, 1.5^2)$	$N(30, 1.5^2)$	$N(30, 1.5^2)$	$N(30, 1.5^2)$
5	9.013	0.165	$N(30, 1.5^2)$	$N(30, 1.5^2)$	$N(30, 1.5^2)$	$N(30, 1.5^2)$
6	10.545	0.170	$N(30, 1^2)$	$1.75t_2 + 30$	$N(30.5, 0.4^2)$	$IG(1, 0.35) + 30$
7	13.200	0.175	$N(30, 1.5^2)$	$N(30, 1.5^2)$	$N(30, 1.5^2)$	$N(30, 1.5^2)$

For both settings, the design matrix \mathbf{X} is a 400×2 matrix, with the first column being the intercept and the second column denoting the group status ($= 1$ for group 1 and -1 for group 2). At a given quantile τ , the model $\mathbf{Y} = \mathbf{X}\mathbf{B}^\tau + \mathbf{E}^\tau$ is fitted to perform FQR. The quantity of interest is the group main effect function $B_2^\tau(t)$, which quantifies the group difference in the τ th quantile at position t .

The true group main effect functions $B_2^\tau(t)$ at various levels of τ in setting (i) and (ii) are demonstrated in Figure 3 (a) and (b). Obvious group differences are present at $\tau = 0.1, 0.2, 0.8, 0.9$ in setting (i), and at $\tau = 0.8, 0.9$ in setting (ii). Figure 3 (c) and (d) show one spectrum per group in a simulated dataset respectively for the two different settings, and it can be seen that each spectrum contains seven peaks that are identically located but allowed different heights across groups.

In setting (i), mean or median regression on the simulated data would detect no group difference because the magnitudes associated with each peak are purposely designed to have identical mean and median between two groups, but the symmetric heavy tailed t_2 leads to obvious group difference in the simulated spectral intensities around the associated peak

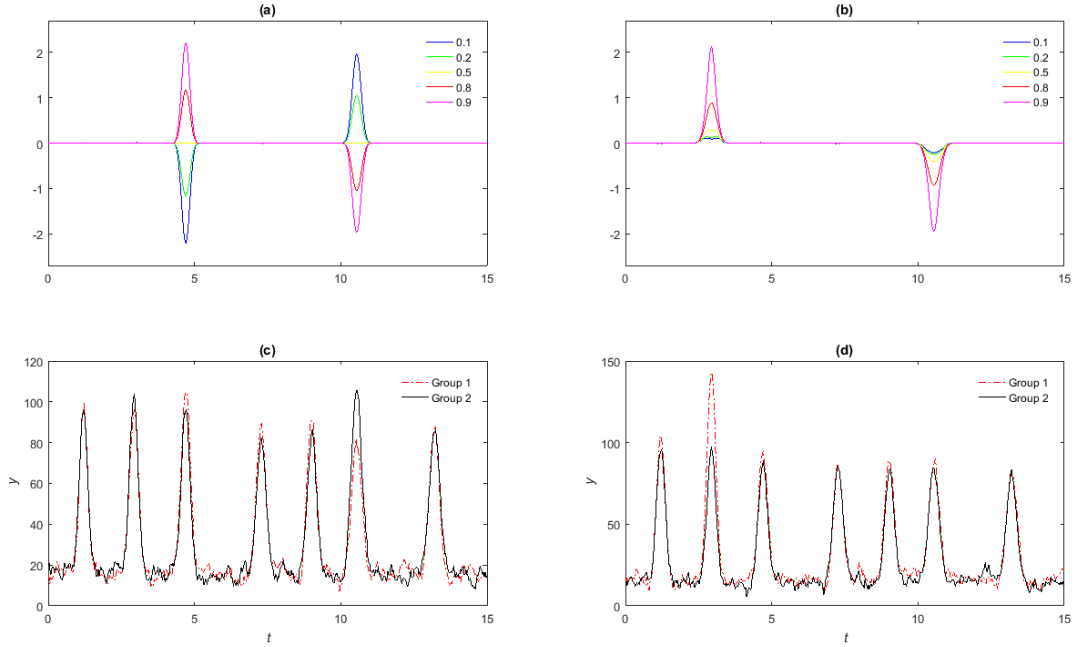


Figure 3: *Group main effect functions and sample curves in simulations.* The true group main effect functions at multiple quantile levels are shown respectively for the symmetric heavy tailed setting (i) in (a), and the right skewed setting (ii) in (b). One simulated curve per group is displayed in (c) for the symmetric heavy tailed setting (i), and in (d) for the right skewed setting (ii).

at more extreme quantiles. In setting (ii), the choice of an inverse Gamma distribution without a finite mean for peak magnitudes renders it theoretically implausible to perform mean regression on the simulated data, while its heavily right skewed nature makes the distributions of the simulated spectral intensities at the associated peak greatly differ in the upper tail but not the median or lower tail across two groups. This scenario was designed to mimic the characteristics of the cancer main effect in the region (5700D, 6000D) that we observed from Figure 2 and described in Section 1.2. These two scenarios are motivated by the setting whereby group differences are evident in the tails but not the center of the distribution, and allow us to examine the performance of our proposed approach in different types of heavy tailed settings.

Bayesian FQR model: We applied our Bayesian FQR model to these simulated data, using a wavelet basis with a Daubechies wavelet with 4 vanishing moments, periodic boundary conditions, and a decomposition level $J = 7$, and a horseshoe regularization prior. Note

that the asymmetric Laplace likelihood, wavelet basis representation, and horseshoe prior were not any part of the data generating process for the simulated data, so our method does not have any unfair advantage over others in its performance.

Alternative approaches: In addition to our proposed Bayesian FQR approach, we also considered a few alternative approaches and assessed their performance, including 1) the naïve Bayesian quantile regression, or Bayesian QR (Yu and Moyeed, 2001) which performs Bayesian quantile regression separately at each location t using the asymmetric Laplace likelihood; 2) the naïve quantile regression, or QR (Koenker, 2005) which does quantile regression at each individual location t by minimizing the check loss function; 3) QR with spline smoothing which smooths the functional coefficients estimated by QR using splines; 4) QR with wavelet denoising which denoises the functional coefficients estimated by QR using wavelets; 5) FDboost which fits a functional linear array model by component-wise gradient boosting. The alternatives based on minimization of the check loss function do not require a likelihood function, while the Bayesian approaches adopt an AL likelihood. To ensure a fair comparison between non-Bayesian and Bayesian methods, we did not simulate data with AL distributed residual errors. We implemented the Bayesian approaches in MATLAB (MATLAB, 2016) and ran each MCMC chain for 8000 iterations, discarding the first 2000 and keeping every 3. The "quantreg" package (Koenker, 2017) in R (R Core Team, 2017) was called to do quantile regression in the approaches 2)-4) and 2000 bootstrap samples were generated per case to perform functional inference. The "FDboost" package (Brockhaus and Ruegamer, 2017) in R was called to implement approach 5).

Evaluation criteria: At each of the quantile levels 0.1, 0.2, 0.5, 0.8 and 0.9, Bayesian FQR model and alternative methods were applied to the simulated datasets to perform FQR. We used SimBaS to identify significantly different regions of the functions between two groups at each quantile. For non-Bayesian approaches, bootstrap samples were generated and used in place of posterior samples to construct simultaneous confidence bands and compute SimBaS. At a given level α , we flagged a location t as significant if its corresponding SimBaS is less than or equal to α , and computed the sensitivity and false positive rate of detecting at least a group difference of $\delta = 0.3$ for each approach, averaging over 100 simulated datasets.

We also evaluated the estimation performance of these methods using a) the integrated mean squared error (IMSE) which measures the variability of the mean estimate around the truth, and b) the integrated variability (IVar) which measures the variability of the posterior samples around the posterior mean estimate for Bayesian approaches, and the variability of bootstrap samples around the mean estimate for bootstrap-based approaches,

also averaging over 100 replications. For a functional parameter $\theta(t)(t \in T)$ with true value $\theta_0(t)$, suppose $\{\theta^{(g)}(t), g = 1, \dots, G\}$ are the G posterior samples for Bayesian approaches, or the G bootstrap samples for bootstrap-based alternatives. $\hat{\theta}(t)$ is the mean estimate of $\theta(t)$ computed by $\hat{\theta}(t) = G^{-1} \sum_{g=1}^G \theta^{(g)}(t)$. IMSE is defined as $\int_T \left\{ \hat{\theta}(t) - \theta_0(t) \right\}^2 dt$, and IVar is defined as $G^{-1} \sum_{g=1}^G \int_T \left\{ \theta^{(g)}(t) - \hat{\theta}(t) \right\}^2 dt$.

Simulation results: The simulation results are presented in Table 2, which summarizes their estimation and inferential performance for each quantile at which the simulated spectra demonstrate *remarkable* group differences as shown in Figure 3 (a) and (b) (results for quantile levels with little or no group differences are not shown), respectively for the symmetric heavy tailed setting (i) and right skewed setting (ii).

The total time to perform FQR on a simulated dataset at the 5 quantile levels on a 64-bit operating system with 2 processors and an RAM of 256GB was about 40 minutes for Bayesian QR, 110 minutes for Bayesian FQR and 70 minutes for the bootstrap-based approaches with or without smoothing. This indicates the Bayesian FQR is computationally scalable to high-dimensional functional datasets along with the competing approaches.

For each quantile τ considered in both settings, the Bayesian FQR model clearly outperformed the naïve Bayesian QR in both estimation accuracy (IMSE) and variability (IVar), and had substantially increased sensitivity at the cost of a slightly higher false positive rate at each of the commonly used levels α . The same conclusions applied to the comparison between the bootstrap-based two-step approaches and their naïve counterpart. These comparisons indicate that regularization of the functional coefficients leads to greatly improved performance in both estimation and inference.

Compared to the two-step alternatives, the Bayesian FQR model had essentially similar estimation accuracy but dramatically reduced estimation variability (IVar) in each case, which resulted in a much tighter simultaneous credible band and considerably increased sensitivity for detecting regions with at least a group difference of $\delta = 0.3$. It is worth noting that at the most commonly chosen threshold $\alpha = 0.05$, all the bootstrap-based approaches have a quite low sensitivity (< 0.3) at each quantile τ considered in each setting. One explanation for the improved performance of the Bayesian FQR is that quantile regression and regularization are done simultaneously in a unified model, in which they can inform each other, while the two-step methods first perform quantile regression independently for each t and only post-smooth the results after model fitting, which in principle can sacrifice efficiency.

τ	Methods	Sensitivity ($\times 10^{-2}$)				False Positive Rate ($\times 10^{-2}$)				IMSE	IVar
	α	0.001	0.01	0.05	0.10	0.001	0.01	0.05	0.10		
0.1	Bayes QR	38.0	49.6	59.3	64.2	0.02	0.05	0.21	0.28	40.3(5.8)	15.1(0.7)
	Bayes FQR	71.8	81.3	86.6	88.9	0.28	1.18	2.65	4.01	24.0(5.3)	4.5(0.4)
	QR	0	0.2	1.3	2.9	0	0	0	0	37.8(5.6)	50.2(3.5)
	QR (+s)	2.6	8.4	23.1	30.9	0	0	0.01	0.03	23.1(5.5)	27.4(3.0)
	QR (+w)	0.1	2.9	16.1	25.4	0	0	0.03	0.06	22.4(5.3)	20.4(3.5)
0.2	Bayes QR	4.9	10.3	16.9	21.1	0.01	0.01	0.03	0.05	26.6(3.4)	14.5(0.3)
	Bayes FQR	37.5	54.7	68.3	72.9	0.06	0.41	1.62	2.72	14.3(3.3)	3.0(0.3)
	QR	0	0	0.8	1.3	0	0	0	0	25.2(3.3)	31.3(0.9)
	QR (+s)	1.1	4.6	10.2	15.3	0	0	0.02	0.03	15.6(3.1)	17.5(0.7)
	QR (+w)	0	0.8	8.5	15.3	0	0	0.01	0.05	13.3(2.8)	11.5(0.7)
0.8	Bayes QR	4.2	10.0	17.3	20.9	0	0	0.02	0.05	26.9(3.8)	14.4(0.3)
	Bayesian FQR	35.5	48.6	61.5	67.4	0.13	0.51	1.76	2.82	14.7(3.4)	3.0(0.2)
	QR	0	0.1	0.3	0.8	0	0	0	0	25.5(3.7)	31.2(0.8)
	QR (+s)	0.7	3.4	9.4	14.2	0	0	0	0	15.8(3.5)	17.4(0.7)
	QR (+w)	0.1	2.2	7.8	12.3	0	0	0.02	0.07	13.5(3.2)	11.5(0.7)
0.9	Bayes QR	35.1	46.8	55.4	59.5	0	0.04	0.17	0.26	41.2(6.7)	15.0(0.6)
	Bayes FQR	66.9	77.3	83.1	85.2	0.24	1.08	2.71	4.00	25.4(6.1)	4.5(0.3)
	QR	0	0	0.7	2.2	0	0	0	0	38.6(6.5)	49.6(2.3)
	QR (+s)	1.7	8.7	20.4	28.9	0	0	0.02	0.03	23.9(6.3)	27.0(2.1)
	QR (+w)	0.2	2.9	14.6	23.2	0	0	0.05	0.11	23.7(5.6)	19.7(2.7)

τ	Methods	Sensitivity ($\times 10^{-2}$)				False Positive Rate ($\times 10^{-2}$)				IMSE	IVar
	α	0.001	0.01	0.05	0.10	0.001	0.01	0.05	0.10		
0.8	Bayes QR	1.2	4.2	8.7	12.7	0	0.01	0.04	0.08	26.6(3.4)	19.9(21.9)
	Bayes FQR	25.4	44.2	57.8	65.0	0.08	0.43	1.55	2.54	14.1(3.2)	3.1(0.3)
	QR	0	0.2	0.4	0.6	0	0	0	0	25.2(3.3)	30.0(0.8)
	QR (+s)	1.0	7.6	19.0	26.1	0	0	0.01	0.04	15.6(3.2)	16.5(0.7)
	QR (+w)	0.7	6.4	26.3	39.5	0	0	0.02	0.09	12.4(2.9)	10.4(0.6)
0.9	Bayes QR	9.7	17.0	25.3	29.8	0.02	0.04	0.12	0.27	45.9(13.8)	37.3(87.0)
	Bayes FQR	43.9	59.1	70.2	74.0	0.30	1.17	2.82	4.04	29.4(11.1)	5.0(0.7)
	QR	0	0	0	0	0	0	0	0	43.6(13.9)	58.1(11.3)
	QR (+s)	0	0.8	5.2	9.5	0	0	0.01	0.01	29.0(13.6)	34.8(10.5)
	QR (+w)	0	0.1	3.7	9.7	0	0	0.02	0.05	26.9(10.3)	27.4(11.4)

Table 2: *Simulation results at selected quantile levels.* For the Bayesian FQR and alternative methods, the sensitivity ($\times 10^{-2}$) and false positive rate ($\times 10^{-2}$) of detecting at least a group difference of $\delta = 0.3$ based on SimBaS at commonly used levels of α , as well as the estimation performance in terms of integrated mean squared error (IMSE) and integrated variability (IVar) with standard deviations in parentheses, are presented for the symmetric heavy tailed setting (i) in the upper table, and the right skewed setting (ii) in the lower table. QR (+s) and QR (+w) refer to the bootstrap-based two-step approaches with spline smoothing and wavelet denoising respectively.

FDboost had difficulty modeling these spiky, spatially heterogeneous data. For example, when applying FDboost with the default arguments to perform FQR on a simulation dataset in the right skewed setting at $\tau = 0.9$, the point estimate of the group main effect function $B_2^{0.9}(t)$ turned out to be identically 0. We suspected this was due to the spline basis, L2 penalty, and the use of gradient boosting for model estimation, which performed variable selection and never selected the predictor coding the highly sparse group difference $B_2^{0.9}(t)$ in any iteration. Although we were able to get a reasonable estimate of $B_2^{0.9}(t)$ with a more suitable choice of arguments, this process required a lot of manual tuning by the user. Additionally, it took 5 minutes to get this reasonable point estimate including the necessary parameter tuning process, suggesting that it would take more than 160 hours to generate 2000 bootstrap samples to perform simultaneous inference using this approach. We repeated this fitting process to 10 replicate datasets which led to the same conclusions each time. Therefore, we decided that FDboost was not appropriate for our simulation settings, and did not apply it to all the simulated datasets or other quantile levels.

4 Functional Quantile Regression for Protein Biomarker Discovery

We applied our Bayesian FQR model using wavelet basis functions, as well as the alternative methods described in Section 3 to perform FQR on the pancreatic cancer mass spectrometry dataset at $\tau = 0.1, 0.25, 0.5, 0.75, 0.9$. We are primarily interested in identifying regions of the mass spectra that significantly differ between the cancer and normal group at each quantile level while adjusting for multiple testing, and comparing the flagged regions across quantiles. For comparative purpose, we also applied the wavelet-based functional mixed model, or WFMM (Morris and Carroll, 2006) to perform functional mean regression to assess which results found by the Bayesian FQR would have been missed had only functional mean regression been done.

Our analysis is focused on the part of the spectra from $t = 5,000$ to $t = 8,000$ Daltons including 1,659 observations per spectrum. To draw meaningful biological conclusions from the mass spectrometry data, it is critical to perform appropriate preprocessing before further statistical analysis (Sorace and Zhan, 2003). The preprocessing steps for MALDI-TOF mass spectrometry data include baseline correction, normalization and denoising, which were performed using the methods described by Coombes et al. (2005). The spectral intensities

can span several orders of magnitude across mass-to-charge ratio t for a given sample, and demonstrate extreme skewness across samples at a given t . To mitigate these issues, we took \log_2 transformation on the mass spectrometry data, which also allows an absolute difference of one on the \log_2 scale to be interpreted as a two-fold change on the original scale. These samples were processed in four different blocks over a span of several months. Previous studies (Baggerly et al., 2003, 2004) show that block effects associated with MALDI-TOF instruments can often be severe, so we estimated and subtracted the block-specific mean from the preprocessed mass spectra to adjust for the block effects. In Figure 1, the right column displays the corresponding preprocessed spectra of the raw spectra in the left column, and this comparison clearly shows the effect of preprocessing.

The design matrix \mathbf{X} for this dataset is a 256×2 matrix, with the first column being the intercept and the second column denoting cancer ($=1$) or normal ($=-1$) status. The models $\mathbf{Y} = \mathbf{X}\mathbf{B}^\tau + \mathbf{E}^\tau$ ($\tau = 0.1, 0.25, 0.5, 0.75, 0.9$) and $\mathbf{Y} = \mathbf{X}\mathbf{B}^{\text{mean}} + \mathbf{E}^{\text{mean}}$ are individually fitted to perform FQR and functional mean regression. The cancer main effect functions $B_2^\tau(t)$ and $B_2^{\text{mean}}(t)$ respectively quantify the difference in the τ th quantile and mean of the \log_2 spectral intensities between cancer and normal groups at the spectral location t . For the Bayesian FQR model, we performed discrete wavelet transform (DWT) using the Daubechies wavelet with 4 vanishing moments, periodic boundary conditions, and a decomposition level $J = 8$. We placed a horseshoe prior on B_{ajh}^* , assuming $\lambda_{ajh} \sim C^+(0, 1)$ and $\psi_{aj} \sim C^+(0, s_a)$, where s_a is a hyperparameter with a vague hyperprior. For the WFMM, we used the same wavelet basis functions to perform DWT and implemented the MCMC procedures as described in Morris et al. (2008) to draw posterior samples. For Bayesian approaches, we ran each MCMC chain for 15000 iterations, discarding the first 5000 and keeping every 5. The trace plots and Geweke diagnostic results of various parameters which are provided in the supplementary materials indicate good mixing of the chains. Using the posterior samples of $B_2^\tau(t)$ or $B_2^{\text{mean}}(t)$, we computed the posterior mean estimate, the $100(1 - \alpha)\%$ simultaneous credible band for $\alpha \in (0, 1)$ and SimBaS of the corresponding functional coefficient at each spectral location t . We flagged t as significantly different in the τ th quantile or mean between the cancer and control groups if its SimBaS is less than or equal to 0.05 and its posterior estimate is greater than $\frac{1}{2} \log_2(1.5)$ in magnitude, corresponding to at least a 1.5-fold change. Such flagging criteria allow us to identify regions that are both statistically and practically significant. For each non-Bayesian method, we generated 2000 bootstrap samples to compute the mean estimate of $B_2^\tau(t)$ and perform functional inference.

To perform FQR on the pancreatic dataset at each quantile level, it took about 1 hour for

Bayesian QR, 4.5 hours for Bayesian FQR and 2.5 hours for each bootstrap-based alternative under the computer setting specified in Section 3. We summarized the mean estimate of $B_2^{\tau}(t)$ ($\tau = 0.1, 0.25, 0.5, 0.75, 0.9$) and the corresponding 95% simultaneous credible band obtained from our Bayesian FQR model and each alternative approach in plots. For the Bayesian FQR, we ran several parallel MCMC chains with different initial values at each quantile level, and obtained essentially the same point estimates and credible bands for $B_2^{\tau}(t)$. At $\tau = 0.1, 0.25, 0.5$, no region was identified as significant by any of the approaches used. At $\tau = 0.75, 0.9$, the regions flagged by each approach were marked on the x-axis in the corresponding plot. All these plots are available in the supplementary materials, and here we highlighted the results for $\tau = 0.9$ produced by our proposed model as well as QR with wavelet denoising, an intuitive alternative that people might use to perform FQR for spiky and irregular functional data, and compared to the functional mean regression results from WFMM in Figure 4.

Both the Bayesian FQR model and QR with wavelet denoising produced an estimate of $B_2^{0.9}(t)$ that are clearly greater in magnitude than $B_2^{\text{mean}}(t)$ in the region (5700D, 6000D), which coincided with what we observed from the empirical quantiles and mean in Figure 2 (a). Both methods identified far more locations than WFMM, which only flagged one narrow contiguous region [5841.5D, 5844.9D]. This suggested that functional mean regression failed to detect most of the spectral locations whose protein expressions differ significantly in the 90th quantile between two groups.

Compared to QR with wavelet denoising, the Bayesian FQR model produced much tighter 95% simultaneous credible band, allowing it to detect more locations. Our model flagged three contiguous regions [5690.6D, 5881.2D] (except for the single location 5706D), [5912.4D, 5957.7D] and [7607.8D, 7619.6D], which covered the two contiguous regions [5704.3D, 5789.8D] and [5817.4D, 5872.6D] flagged by QR with wavelet denoising but included many more locations. Notably, the regions [5912.4D, 5957.7D] and [7607.8D, 7619.6D] were identified by our model but entirely missed by the two-step approach. In addition, the two-step alternative appeared to have an over-smoothed estimate of $B_2^{0.9}(t)$. For example, the Bayesian FQR detected three adjacent sharp peaks located at 5696D, 5745D and 5761D, whereas the two-step approach only recognized one broader peak in this region; the Bayesian FQR flagged two separate peaks at 5824D and 5842D, but the two-step alternative seemed to over-smooth them into one single peak.

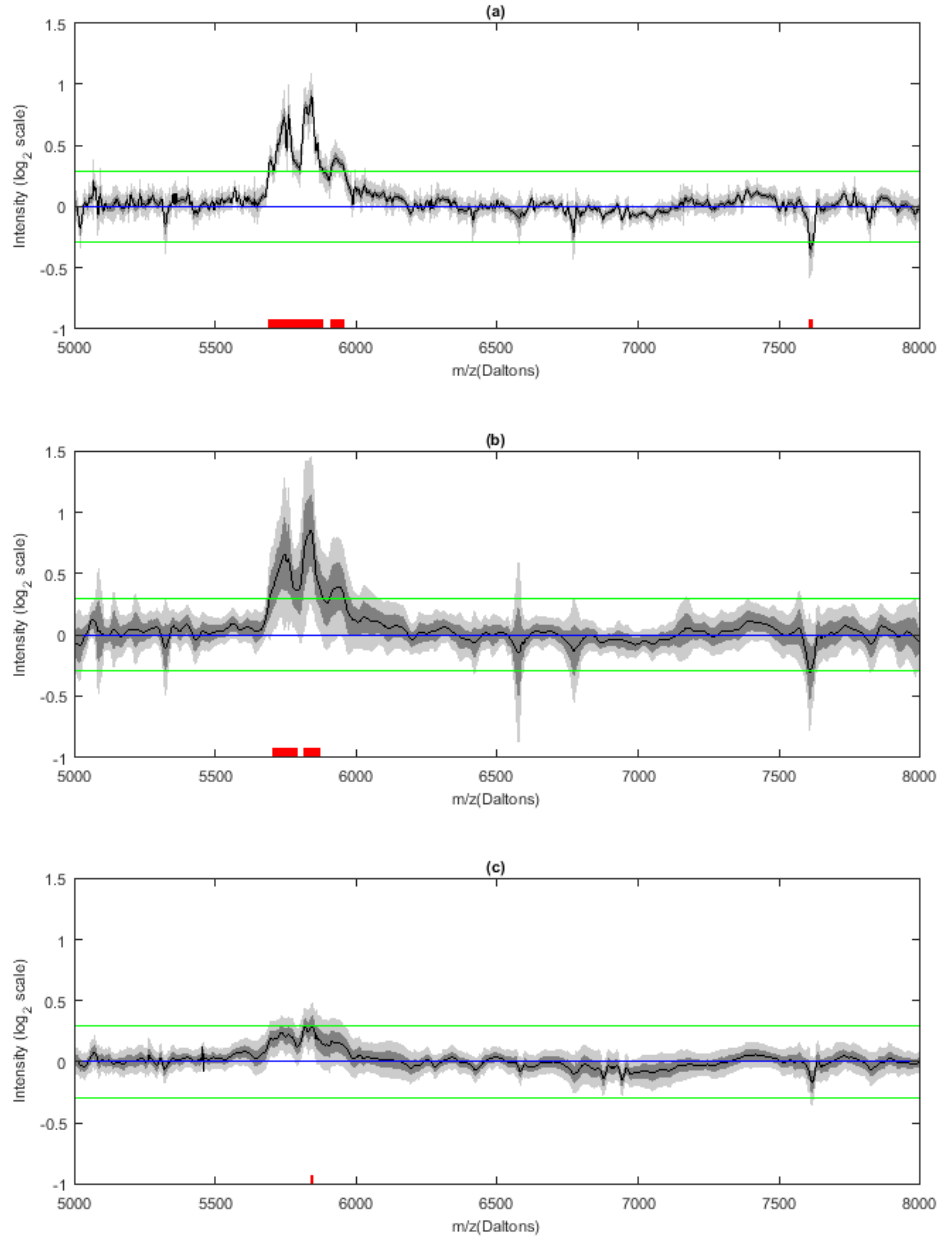


Figure 4: *Estimated cancer main effect functions for the pancreatic cancer dataset.* (a) $B_2^{0.9}(t)$ estimated by the Bayesian FQR model. (b) $B_2^{0.9}(t)$ estimated by the bootstrap-based QR with wavelet denoising. (c) $B_2^{\text{mean}}(t)$ estimated by the WFMM model. The estimated cancer main effects are plotted on \log_2 scale along with the corresponding 95% pointwise and simultaneous credible bands. A spectral location is flagged as significant and marked on the x-axis if its SimBaS is less than or equal to 0.05 and the estimate corresponds to at least 1.5-fold change indicated by the two horizontal lines.

The proteins corresponding to the regions flagged by our model might serve as potential biomarkers of pancreatic cancer. We assessed the possible protein identities of the flagged spectral regions using TagIdent ([Gasteiger et al., 2005](#)), an online protein identification tool that can create a list of proteins from one or more organisms within a range of the pH and mass-to-charge ratio specified by the user. In particular, the flagged region [5690.6D, 5881.2D] may correspond to basic salivary proline-rich peptide IB-7 (5769D) and peptide IB-8c (5843D) coded by PRB2 gene, whose single-nucleotide polymorphism (SNP) has been found to be significantly associated with the response of pancreatic cancer patients to gemcitabine based on a genome-wide association study ([Innocenti et al., 2012](#)). The flagged region [5912.4D, 5957.7D] may correspond to a variant of transient receptor potential cation channel subfamily M member 8 (TRPM8, 5940D) which has been reported to be aberrantly expressed in pancreatic adenocarcinoma and have the potential to become a clinical biomarker and therapeutic target for pancreatic cancer ([Yee et al., 2012](#)). The narrow region [7607.8D, 7619.6D] which was flagged only by our approach may correspond to stromal cell-derived factor 1 (SDF1, 7610D) coded by CXCL12 gene, and it has been discovered that CXCL12-CXCR7 signaling axis is significantly associated with the invasive potential of pancreatic tumor cells and the overall survival of pancreatic cancer patients ([Guo et al., 2016](#)). To definitively find the protein identities of these spectral regions it would be necessary to conduct a tandem mass spectrometry (MS/MS) experiment ([Kinter and Sherman, 2005](#); [Deutsch et al., 2008](#)), but this is beyond the scope of our current study.

5 Discussion

In this paper, we introduced a fully Bayesian approach to perform quantile regression on functional responses. The existing work on functional response regression has focused predominantly on mean regression. However, sometimes predictors may not strongly influence the conditional mean of functional responses, but other aspects of their conditional distributions instead, as illustrated by our analysis of the motivating pancreatic cancer mass spectrometry dataset. In this case, performing functional quantile regression to delineate the relationship between functional responses and predictors is warranted. This can straightforwardly be done by performing quantile regression at each individual functional location, but as we demonstrate this is not an efficient strategy since it fails to borrow strength from nearby functional locations. Our proposed approach is able to borrow strength across nearby locations by representing the functional coefficients with appropriate basis functions, and in-

duce adaptive penalization on the basis coefficients by placing a global-local shrinkage prior. Our framework is very flexible in that it allows different types of basis transform and continuous shrinkage priors, which are chosen based on the characteristics of functional data. We assumed the conditional quantile to be linear in the covariates in this paper, but our model can be easily extended to model nonparametric effect of covariates (Fasiolo et al., 2018) by using spline design matrix. We developed an efficient data augmented block Gibbs sampler to do posterior computation, which can be implemented automatically without tuning parameters and scale up well to moderately-sized functional data consisting of hundreds of observations per curve. The posterior samples can be used to perform Bayesian estimation and inference on any parameter of interest.

We applied our approach to perform FQR on the pancreatic cancer MALDI-TOF data set at multiple quantile levels, using wavelet basis functions and a horseshoe prior on the wavelet coefficients. Compared to WFMM, our Bayesian FQR model identified many more spectral locations in the range [5000D, 8000D], which correspond to proteins whose intensity levels differ significantly in the 90th quantile but not the mean between the cancer and normal populations. While we chose to use wavelets and a horseshoe prior to present our approach, which are well-suited for the highly spiky and irregular mass spectrometry data, other basis functions including functional principal components, Fourier series and splines and a great variety of shrinkage priors can also be used in this framework, as elaborated in Section 2.1. In addition, our framework can accommodate multi-dimensional functional data by applying a multi-dimensional basis transform. For example, a 2D wavelet transform can be applied to the 2D mass spectrometry data collected in LC-MS experiment (Zhang et al., 2009; Liao et al., 2014), so this approach can be used to perform FQR on data from these assays as well.

We simulated functional data with Gaussian shaped peaks to mimic mass spectra, evaluated the performance of our method under different simulation settings and compared to simpler alternatives that people might use to perform FQR. Our approach consistently outperformed the naïve Bayesian quantile regression in both estimation and inference, showing that it is clearly inefficient to ignore the functional nature of data and do quantile regression separately for each location. In addition to borrowing strength, our model adopted a sparsity prior that can effectively shrink small wavelet coefficients to zero and avoid attenuation of large coefficients, minimizing bias and substantially reducing variation in parameter estimation. Compared to the bootstrap-based two-step alternatives that seemed intuitively appealing, our approach achieved comparable estimation accuracy (IMSE) but considerably

smaller variability (IVar), which lead to much tighter simultaneous credible band and greatly improved sensitivity for identifying regions with significant group differences at particular quantile levels.

The improvement of our Bayesian FQR model over the bootstrap-based two-step alternatives could be explained by the following facts. First, quantile regression and penalization of functional coefficients are performed jointly in a unified manner in our Bayesian framework, which we believe to have the potential to achieve more adaptive regularization than performing them separately as done in the two-step approaches. Second, given the connection between the asymmetric Laplace distribution and the check loss function, the likelihood term in our Bayesian model corresponds to a more flexible loss function than the two-step alternatives, which could contribute to its superior performance. To be more specific, conditioning on $\sigma(t_l)$ and integrating out $\xi_i(t_l)$, the likelihood part in our Bayesian formulation is a weighted sum of check loss over t . The weights $\frac{1}{\sigma(t_l)} (l = 1, \dots, T)$ are updated at each MCMC iteration and marginalized over their posterior distributions. In contrast, the check loss functions of the non-Bayesian alternatives have an equal weight over t . While our Bayesian hierarchical model is convenient to implement, it would be very challenging to fit a non-Bayesian counterpart with the same flexibility and complexity, and yield estimation and inference of \mathbf{B} while choosing the scale parameters $\sigma(t_l)$ and various penalization parameters λ_{ajh} and ψ_{aj} by cross-validation.

To our knowledge, there exists very limited work on FQR in the statistical literature. Based on our simulations, the framework proposed by [Brockhaus et al. \(2015\)](#) appears to work satisfactorily for simple and homogeneous functions sampled on a relatively sparse grid, but not as well for high-dimensional spiky and complex functions in terms of coefficient estimation and computational feasibility. In addition, their framework does not automatically yield pointwise or joint inference.

We proposed a highly flexible and computationally tractable Bayesian framework to perform quantile regression for functional responses, but there is still room for improvement. Our modeling approach is built for functional data sampled on a sufficiently fine grid where interpolation can be reasonably used to obtain a common grid for subjects. Further adaptations of our model and code would be required to handle functional data sampled on sparse grids that vary across subjects, and are left for future work. Also, we assumed independent residual errors across t for the functional observations, but observations from nearby functional locations are typically correlated with each other. The assumption of independent errors may tend to make the inference more conservative, thus further efficiency and power

gains are possible if within-function correlations could be accommodated (Morris, 2017). However, the tractability of our proposed framework breaks down if we are to model this dependence structure, and this challenging problem has *never* yet been addressed in the existing literature to our best knowledge. We leave it as a topic for future investigation to model functionally correlated residual errors in high dimensional FQR with tractable computation. It should be pointed out that our proposed approach beats all the simpler methods that people might use to perform FQR as shown by the simulations, so our work is still a significant step forward in this area. In addition, an asymmetric Laplace likelihood is used in our framework due to its computational efficiency, and further theoretical studies on the properties of the posterior inference based on this possibly misspecified working likelihood would be insightful (Yang et al., 2016; Syring and Martin, 2018).

SUPPLEMENTARY MATERIAL

The supplementary materials include mathematical details of the MCMC sampling procedure and additional results of mass spectrometry data application. The pancreatic cancer mass spectrometry dataset, simulation datasets and the related MATLAB and R code are available at <https://github.com/MorrisStatLab/FunctionalQuantileRegression>.

References

- Baggerly, K. A., J. S. Morris, and K. R. Coombes (2004). Reproducibility of seldi-tof protein patterns in serum: comparing datasets from different experiments. *Bioinformatics* 20(5), 777–785.
- Baggerly, K. A., J. S. Morris, J. Wang, D. Gold, L.-C. Xiao, and K. R. Coombes (2003). A comprehensive approach to the analysis of matrix-assisted laser desorption/ionization-time of flight proteomics spectra from serum samples. *Proteomics* 3(9), 1667–1672.
- Brockhaus, S. and D. Ruegamer (2017). *FDboost: Boosting Functional Regression Models*.
- Brockhaus, S., F. Scheipl, T. Hothorn, and S. Greven (2015). The functional linear array model. *Statistical Modelling* 15(3), 279–300.
- Cardot, H., C. Crambes, and P. Sarda (2005). Quantile regression when the covariates are functions. *Nonparametric Statistics* 17(7), 841–856.

- Carvalho, C. M., N. G. Polson, and J. G. Scott (2009). Handling sparsity via the horseshoe. In *Artificial Intelligence and Statistics*, pp. 73–80.
- Carvalho, C. M., N. G. Polson, and J. G. Scott (2010). The horseshoe estimator for sparse signals. *Biometrika* 97(2), 465–480.
- Chen, K. and H.-G. Müller (2012). Conditional quantile analysis when covariates are functions, with application to growth data. *Journal of the Royal Statistical Society: Series B (Statistical Methodology)* 74(1), 67–89.
- Coombes, K. R., S. Tsavachidis, J. S. Morris, K. A. Baggerly, M.-C. Hung, and H. M. Kuerer (2005). Improved peak detection and quantification of mass spectrometry data acquired from surface-enhanced laser desorption and ionization by denoising spectra with the undecimated discrete wavelet transform. *Proteomics* 5(16), 4107–4117.
- Deutsch, E. W., H. Lam, and R. Aebersold (2008). Data analysis and bioinformatics tools for tandem mass spectrometry in proteomics. *Physiological genomics* 33(1), 18–25.
- Fasiolo, M., Y. Goude, R. Nedellec, and S. N. Wood (2018). Fast calibrated additive quantile regression. *arXiv preprint arXiv:1707.03307*.
- Ferraty, F., A. Rabhi, and P. Vieu (2005). Conditional quantiles for dependent functional data with application to the climatic *El Niño* phenomenon. *Sankhyā: The Indian Journal of Statistics* 67(2), 378–398.
- Gasteiger, E., C. Hoogland, A. Gattiker, M. R. Wilkins, R. D. Appel, A. Bairoch, et al. (2005). Protein identification and analysis tools on the expasy server. In *The proteomics protocols handbook*, pp. 571–607. Springer.
- Guo, J.-C., J. Li, L. Zhou, J.-Y. Yang, Z.-G. Zhang, Z.-Y. Liang, W.-X. Zhou, L. You, T.-P. Zhang, and Y.-P. Zhao (2016). Cxcl12-cxcr7 axis contributes to the invasive phenotype of pancreatic cancer. *Oncotarget* 7(38), 62006.
- Innocenti, F., K. Owzar, N. L. Cox, P. Evans, M. Kubo, H. Zembutsu, C. Jiang, D. Hollis, T. Mushiroda, L. Li, et al. (2012). A genome-wide association study of overall survival in pancreatic cancer patients treated with gemcitabine in calgb 80303. *Clinical Cancer Research* 18(2), 577–584.

- Kato, K. (2012). Estimation in functional linear quantile regression. *The Annals of Statistics* 40(6), 3108–3136.
- Kinter, M. and N. E. Sherman (2005). *Protein sequencing and identification using tandem mass spectrometry*, Volume 9. John Wiley & Sons.
- Koenker, R. (2005). *Quantile Regression*. Cambridge University Press.
- Koenker, R. (2017). *quantreg: Quantile Regression*. R package version 5.33.
- Koenker, R. and G. Bassett Jr (1978). Regression quantiles. *Econometrica: journal of the Econometric Society*, 33–50.
- Koomen, J. M., L. N. Shih, K. R. Coombes, D. Li, L.-c. Xiao, I. J. Fidler, J. L. Abbruzzese, and R. Kobayashi (2005). Plasma protein profiling for diagnosis of pancreatic cancer reveals the presence of host response proteins. *Clinical Cancer Research* 11(3), 1110–1118.
- Li, M., K. Wang, A. Maity, and A.-M. Staicu (2016). Inference in functional linear quantile regression. *arXiv preprint arXiv:1602.08793*.
- Liao, H., E. Moschidis, I. Riba-Garcia, Y. Zhang, R. D. Unwin, J. S. Morris, J. Graham, and A. W. Dowsey (2014). A new paradigm for clinical biomarker discovery and screening with mass spectrometry through biomedical image analysis principles. In *Biomedical Imaging (ISBI), 2014 IEEE 11th International Symposium on*, pp. 1332–1335. IEEE.
- Lum, K., A. E. Gelfand, et al. (2012). Spatial quantile multiple regression using the asymmetric laplace process. *Bayesian Analysis* 7(2), 235–258.
- MATLAB (2016). *version 9.1 (R2016b)*. Natick, Massachusetts: The MathWorks Inc.
- Meyer, M. J., B. A. Coull, F. Versace, P. Cinciripini, and J. S. Morris (2015). Bayesian function-on-function regression for multilevel functional data. *Biometrics* 71(3), 563–574.
- Morris, J. S. (2012). Statistical methods for proteomic biomarker discovery based on feature extraction or functional modeling approaches. *Statistics and its Interface* 5(1), 117.
- Morris, J. S. (2015). Functional regression. *Annual Review of Statistics and Its Application* 2, 321–359.

- Morris, J. S. (2017). Comparison and contrast of two general functional regression modelling frameworks. *Statistical modelling* 17(1-2), 59–85.
- Morris, J. S., P. J. Brown, R. C. Herrick, K. A. Baggerly, and K. R. Coombes (2008). Bayesian analysis of mass spectrometry proteomic data using wavelet-based functional mixed models. *Biometrics* 64(2), 479–489.
- Morris, J. S. and R. J. Carroll (2006). Wavelet-based functional mixed models. *Journal of the Royal Statistical Society: Series B (Statistical Methodology)* 68(2), 179–199.
- Polson, N. G. and J. G. Scott (2010). Shrink globally, act locally: Sparse bayesian regularization and prediction. *Bayesian statistics 9*, 501–538.
- R Core Team (2017). *R: A Language and Environment for Statistical Computing*. Vienna, Austria: R Foundation for Statistical Computing.
- Reed, C. and K. Yu (2009). A partially collapsed gibbs sampler for bayesian quantile regression.
- Ruppert, D., M. Wand, and R. Carroll (2003). *Semiparametric regression*. New York: Cambridge University Press.
- Sorace, J. M. and M. Zhan (2003). A data review and re-assessment of ovarian cancer serum proteomic profiling. *BMC bioinformatics* 4(1), 24.
- Syring, N. and R. Martin (2018). Calibrating general posterior credible regions. *arXiv preprint arXiv:1509.00922v4*.
- Yang, Y., H. J. Wang, and X. He (2016). Posterior inference in bayesian quantile regression with asymmetric laplace likelihood. *International Statistical Review* 84(3), 327–344.
- Yee, N. S., A. S. Chan, J. D. Yee, and R. K. Yee (2012). Trpm7 and trpm8 ion channels in pancreatic adenocarcinoma: potential roles as cancer biomarkers and targets. *Scientifica* 2012.
- Yu, K. and R. A. Moyeed (2001). Bayesian quantile regression. *Statistics & Probability Letters* 54(4), 437–447.
- Zhang, J., E. Gonzalez, T. Hestilow, W. Haskins, and Y. Huang (2009). Review of peak detection algorithms in liquid-chromatography-mass spectrometry. *Current genomics* 10(6), 388.

Function-on-Scalar Quantile Regression with Application to Mass Spectrometry Proteomics Data: Supplementary Materials

Yusha Liu^{*}, Meng Li^{*} and Jeffrey S. Morris[†]

^{}Department of Statistics, Rice University*

[†]Department of Biostatistics, University of Texas MD Anderson Cancer Center

August 31, 2018

This document includes mathematical details of the MCMC sampling procedure, additional results of mass spectrometry data application, and implementation details of FDboost package.

1 Posterior computation via MCMC sampling

1.1 Detailed Gibbs sampling procedures for horseshor prior on basis coefficients

We detail the Gibbs sampling procedures to draw posterior samples of the parameters in model (4) in the main paper from their full conditional posterior distributions. We describe how to update the global and local shrinkage parameters if a horseshoe prior is placed on B_{ajh}^* , which is used in simulation studies and real data application in this paper. Specifically, it is assumed that $\lambda_{ajh} \sim C^+(0, 1)$ and $\psi_{aj} \sim C^+(0, s_a)$, where s_a can either be fixed as 1 (Carvalho et al., 2009), or treated as a hyperparameter and given a vague hyperprior. Here we choose to assign s_a^2 a vague inverse Gamma hyperprior with a mode of 1. To update λ_{ajh} and ψ_{aj} , we make use of the inverse Gamma scale mixture representation for the half Cauchy distribution (Makalic and Schmidt, 2016) and introduce the auxiliary variables ν_{ajh} and γ_{aj} , i.e.,

$$\begin{aligned} \lambda_{ajh}^2 | \nu_{ajh} &\sim \text{inverse Gamma} \left(\frac{1}{2}, \frac{1}{\nu_{ajh}} \right), & \nu_{ajh} &\sim \text{inverse Gamma} \left(\frac{1}{2}, 1 \right); \\ \psi_{aj}^2 | \gamma_{aj} &\sim \text{inverse Gamma} \left(\frac{1}{2}, \frac{1}{\gamma_{aj}} \right), & \gamma_{aj} &\sim \text{inverse Gamma} \left(\frac{1}{2}, \frac{1}{s_a^2} \right). \end{aligned}$$

The parameters to be updated are $\{B_a(t_l)\}$, $\{\sigma(t_l)\}$, $\{\xi_i(t_l)\}$, $\{B_{ajh}^*\}$, $\{\lambda_{ajh}\}$, $\{\nu_{ajh}\}$, $\{\psi_{aj}\}$, $\{\gamma_{aj}\}$ and $\{s_a\}$. For initialization, we compute the initial values of $B_a(t)$ in model (1) in the main paper by obtaining their maximum likelihood estimates (MLE) assuming *i.i.d.* Gaussian errors for $E_i(t)$, and initialize \mathbf{B}^* using $\mathbf{B}^* = \mathbf{B}\Phi^-$, where $\Phi^- = \Phi'(\Phi\Phi')^{-1}$ is the Moore-Penrose generalized inverse matrix of Φ in equation (5) in the main paper. The initial value of s_a is set to 1, and the initial values of λ_{ajh} , ν_{ajh} , ψ_{aj} and γ_{aj} are obtained by sampling from their prior distributions respectively. Below are the steps of posterior sampling with derivation.

1. For each position l , $\sigma(t_l)$ has a vague prior of inverse Gamma $(\alpha_{\sigma_l}, \beta_{\sigma_l})$. Update $\sigma(t_l)$ by $(\sigma(t_l) | \mathbf{B}(t_l), \mathbf{y}(t_l), \alpha_{\sigma_l}, \beta_{\sigma_l}) \sim \text{inverse Gamma} \left(N + \alpha_{\sigma_l}, \sum_{i=1}^N \rho_{\tau} (Y_i(t_l) - \mathbf{X}_i' \mathbf{B}(t_l)) + \beta_{\sigma_l} \right)$. Note that the conditional distributions of $\sigma(t_l)$ are obtained by integrating out latent variables $\xi_i(t_l)$, leading to a partially collapsed Gibbs step with improved mixing properties.

2. For each subject i and position l , update $\xi_i(t_l)$ by $(1/\xi_i(t_l) \mid \mathbf{B}(t_l), Y_i(t_l), \sigma(t_l)) \sim$ inverse Gaussian $(1/\{\tau(1-\tau) | Y_i(t_l) - \mathbf{X}'_i \mathbf{B}(t_l) | \}, 1/\{2\tau(1-\tau)\sigma(t_l)\})$.
3. For each covariate a , update \mathbf{B}_a^* from $f(\mathbf{B}_a^* \mid \mathbf{B}_{-a}^*, \mathbf{Y}, \boldsymbol{\sigma}, \boldsymbol{\xi}, \boldsymbol{\lambda}_a, \boldsymbol{\psi}_a)$, where \mathbf{B}_{-a}^* is the $(p-1) \times K$ matrix of basis coefficients with the a^{th} row excluded from \mathbf{B}^* , $\boldsymbol{\xi}$ is the $N \times T$ matrix of latent variables with $\boldsymbol{\xi}(i, l) = \xi_i(t_l)$, $\boldsymbol{\sigma} = \{\sigma(t_l)\}_l$, $\boldsymbol{\lambda}_a = \{\lambda_{ajh}\}_{j,h}$, $\boldsymbol{\psi}_a = \{\psi_{aj}\}_j$. Projection of \mathbf{B} into the basis space is performed in this step, which can be computed by $\mathbf{B}^* = \mathbf{B}\Phi^-$. It turns out that

$$(\mathbf{B}_a^* \mid \mathbf{Y}, \mathbf{B}_{-a}^*, \boldsymbol{\sigma}, \boldsymbol{\xi}, \boldsymbol{\lambda}_a, \boldsymbol{\psi}_a) \sim MVN(\mu_a, \Lambda_a),$$

for some μ_a and Λ_a defined below.

We next elaborate the derivation of the full conditional distributions of \mathbf{B}^* . For each subject i and position l , let $\tilde{Y}_i(t_l) = Y_i(t_l) - \frac{1-2\tau}{\tau(1-\tau)}\xi_i(t_l)$, we can rewrite model (4) in the main paper as

$$\tilde{Y}_i(t_l) = \mathbf{X}'_i \mathbf{B}(t_l) + \varepsilon_i(t_l), \quad \varepsilon_i(t_l) \sim N\left(0, \frac{2\xi_i(t_l)\sigma(t_l)}{\tau(1-\tau)}\right),$$

or in matrix form,

$$\tilde{\mathbf{Y}} = \mathbf{X}\mathbf{B} + \boldsymbol{\varepsilon}, \quad \boldsymbol{\varepsilon}(t_l) \sim MVN(0, \boldsymbol{\Xi}_l),$$

where $\boldsymbol{\Xi}_l = \text{diag}\left\{\frac{2\xi_i(t_l)\sigma(t_l)}{\tau(1-\tau)}\right\}_{i=1}^N$. We rescale each column in the foregoing equation by premultiplying by $\boldsymbol{\Xi}_l^{-\frac{1}{2}}$, and obtain

$$\tilde{\mathbf{y}}_l^+ = \mathbf{X}_l^+ \mathbf{B}(t_l) + \boldsymbol{\varepsilon}_l^+, \quad \boldsymbol{\varepsilon}_l^+ \sim MVN(0, \mathbf{I}_N), \quad (1)$$

where $\tilde{\mathbf{y}}_l^+ = \boldsymbol{\Xi}_l^{-\frac{1}{2}}\tilde{\mathbf{y}}(t_l)$, $\mathbf{X}_l^+ = \boldsymbol{\Xi}_l^{-\frac{1}{2}}\mathbf{X}$, and $\boldsymbol{\varepsilon}_l^+ = \boldsymbol{\Xi}_l^{-\frac{1}{2}}\boldsymbol{\varepsilon}(t_l)$ are the rescaled versions of the responses, design matrix and residuals for position t_l . Let $\tilde{\mathbf{y}}_l^{++} = \tilde{\mathbf{y}}_l^+ - \mathbf{X}_{(-a)l}^+ \mathbf{B}_{(-a)}(t_l)$, where \mathbf{X}_{al}^+ represents the a^{th} column of \mathbf{X}_l^+ and $\mathbf{X}_{(-a)l}^+$ is \mathbf{X}_l^+ with the a^{th} column removed, $\hat{B}_a(t_l) = \left(\mathbf{X}_{al}^{+'} \mathbf{X}_{al}^+\right)^{-1} \mathbf{X}_{al}^{+'} \tilde{\mathbf{y}}_l^{++}$, $V_{al} = \left(\mathbf{X}_{al}^{+'} \mathbf{X}_{al}^+\right)^{-1}$, $\hat{\mathbf{B}}_a = \left(\hat{B}_a(t_1), \dots, \hat{B}_a(t_T)\right)'$, $\mathbf{V}_a = \text{diag}\{V_{al}\}_{l=1}^T$, $\mathbf{v}_a = \text{diag}\{\lambda_{ajh}^2 \psi_{aj}^2\}_{j,h}$, $\mathbf{B}_a^* = \Phi^{-'} \mathbf{B}_a$, $\hat{\mathbf{B}}_a^* = \Phi^{-'} \hat{\mathbf{B}}_a$, and $\boldsymbol{\Sigma}_a = \Phi^{-'} \mathbf{V}_a \Phi^-$. Note that $\hat{B}_a(t_l)$ is the MLE of $B_a(t_l)$ in model (1) conditional on $\mathbf{B}_{-a}(t_l)$, the scale parameter $\sigma(t_l)$ and the latent variables $\{\xi_i(t_l)\}_{i=1}^N$; V_{al} is the variance of this MLE. Assuming independent $\boldsymbol{\varepsilon}_l^+$ across l as done in our model

and projecting into the basis space, $\hat{\mathbf{B}}_a^*$ takes the form of MLE of \mathbf{B}_a^* conditional on \mathbf{B}_{-a}^* and scale parameters; Σ_a is the covariance matrix of $\hat{\mathbf{B}}_a^*$.

Then the conditional distributions of \mathbf{B}^* are obtained by

$$\begin{aligned}
& f(\mathbf{B}_a^* \mid \mathbf{Y}, \mathbf{B}_{-a}^*, \boldsymbol{\sigma}, \boldsymbol{\xi}, \boldsymbol{\lambda}_a, \boldsymbol{\psi}_a) \propto f(\mathbf{Y} \mid \mathbf{B}_a^*, \mathbf{B}_{-a}^*, \boldsymbol{\sigma}, \boldsymbol{\xi}) f(\mathbf{B}_a^* \mid \boldsymbol{\lambda}_a, \boldsymbol{\psi}_a) \\
& \propto \prod_{l=1}^T f(\mathbf{y}(t_l) \mid \mathbf{B}(t_l), \boldsymbol{\sigma}(t_l), \boldsymbol{\xi}(t_l)) f(\mathbf{B}_a^* \mid \boldsymbol{\lambda}_a, \boldsymbol{\psi}_a) \\
& \propto \prod_{l=1}^T \exp \left[-\frac{1}{2} (\tilde{\mathbf{y}}_l^+ - \mathbf{X}_l^+ \mathbf{B}(t_l))' \mathbf{I}_N^{-1} (\tilde{\mathbf{y}}_l^+ - \mathbf{X}_l^+ \mathbf{B}(t_l)) \right] f(\mathbf{B}_a^* \mid \boldsymbol{\lambda}_a, \boldsymbol{\psi}_a) \\
& \propto \prod_{l=1}^T \exp \left[-\frac{1}{2} (\tilde{\mathbf{y}}_l^{++} - \mathbf{X}_{al}^+ B_a(t_l))' (\tilde{\mathbf{y}}_l^{++} - \mathbf{X}_{al}^+ B_a(t_l)) \right] \prod_{j,h} f(B_{ajh}^* \mid \lambda_{ajh}, \psi_{aj}) \\
& \propto \prod_{l=1}^T \exp \left[-\frac{1}{2} \frac{(B_a(t_l) - \hat{B}_a(t_l))^2}{V_{al}} \right] \prod_{j,h} \exp \left[-\frac{1}{2} \frac{B_{ajh}^{*2}}{\lambda_{ajh}^2 \psi_{aj}^2} \right] \\
& \propto \exp \left[-\frac{1}{2} (\mathbf{B}_a - \hat{\mathbf{B}}_a)' \mathbf{V}_a^{-1} (\mathbf{B}_a - \hat{\mathbf{B}}_a) \right] \exp \left[-\frac{1}{2} \mathbf{B}_a' \mathbf{v}_a^{-1} \mathbf{B}_a \right] \\
& \propto \exp \left[-\frac{1}{2} (\mathbf{B}_a^* - \hat{\mathbf{B}}_a^*)' \Sigma_a^{-1} (\mathbf{B}_a^* - \hat{\mathbf{B}}_a^*) \right] \exp \left[-\frac{1}{2} \mathbf{B}_a^{*'} \mathbf{v}_a^{-1} \mathbf{B}_a^* \right] \\
& \propto \exp \left[-\frac{1}{2} (\mathbf{B}_a^* - \boldsymbol{\mu}_a)' \Lambda_a^{-1} (\mathbf{B}_a^* - \boldsymbol{\mu}_a) \right],
\end{aligned}$$

$\boldsymbol{\mu}_a = \left[\mathbf{I}_K - \Sigma_a \mathbf{v}_a^{-1} (\mathbf{I}_K + \Sigma_a \mathbf{v}_a^{-1})^{-1} \right] \hat{\mathbf{B}}_a^*$ and $\Lambda_a = \left[\mathbf{I}_K - \Sigma_a \mathbf{v}_a^{-1} (\mathbf{I}_K + \Sigma_a \mathbf{v}_a^{-1})^{-1} \right] \Sigma_a$. The conditional mean $\boldsymbol{\mu}_a$ of \mathbf{B}_a^* is a product of the unshrunk estimator $\hat{\mathbf{B}}_a^*$ and the shrinkage factor $\mathbf{I}_K - \Sigma_a \mathbf{v}_a^{-1} (\mathbf{I}_K + \Sigma_a \mathbf{v}_a^{-1})^{-1}$, which includes the regularization parameters through \mathbf{v}_a . Similarly, the conditional covariance matrix Λ_a of \mathbf{B}_a^* is a product of this shrinkage factor and the unshrunk estimator Σ_a .

4. The updates of $\lambda_{ajh}, \nu_{ajh}, \psi_{aj}, \gamma_{aj}$ follow the standard procedures for the horseshoe prior. For each covariate a and basis index j, h , update λ_{ajh}^2 and ν_{ajh} by

$$\begin{aligned}
(\lambda_{ajh}^2 \mid B_{ajh}^*, \nu_{ajh}, \psi_{aj}) & \sim \text{inverse Gamma} \left(1, \frac{1}{2} \frac{B_{ajh}^{*2}}{\psi_{aj}^2} + \frac{1}{\nu_{ajh}} \right), \\
(\nu_{ajh} \mid \lambda_{ajh}) & \sim \text{inverse Gamma} \left(1, \frac{1}{\lambda_{ajh}^2} + 1 \right).
\end{aligned}$$

For each covariate a and regularization subset j , update ψ_{aj}^2 and γ_{aj} by

$$\begin{aligned} (\psi_{aj}^2 \mid \mathbf{B}_a^*, \boldsymbol{\lambda}_a, \gamma_{aj}) &\sim \text{inverse Gamma} \left(\frac{1}{2}H_j + \frac{1}{2}, \sum_{h=1}^{H_j} \frac{B_{ajh}^{*2}}{2\lambda_{ajh}^2} + \frac{1}{\gamma_{aj}} \right), \\ (\gamma_{aj} \mid \psi_{aj}^2, s_a) &\sim \text{inverse Gamma} \left(1, \frac{1}{\psi_{aj}^2} + \frac{1}{s_a^2} \right). \end{aligned}$$

For each covariate a , the hyperparameter s_a^2 has a vague hyperprior of inverse Gamma $(\alpha_{s_a^2}, \beta_{s_a^2})$ with the mode at 1. Update s_a^2 by

$$(s_a^2 \mid \boldsymbol{\gamma}_a, \alpha_{s_a^2}, \beta_{s_a^2}) \sim \text{inverse Gamma} \left(\frac{J}{2} + \alpha_{s_a^2}, \sum_{j=1}^J \frac{1}{\gamma_{aj}} + \beta_{s_a^2} \right).$$

5. Update \mathbf{B} by $\mathbf{B} = \mathbf{B}^* \boldsymbol{\Phi}$.

1.2 Other global-local shrinkage priors on basis coefficients

It is straightforward to modify the sampling step 4 in Section 1.1 to accommodate other computationally tractable global-local shrinkage priors, including the Gaussian prior, Laplace prior, Normal-Gamma Prior (Griffin et al., 2010), and Dirichlet-Laplace prior (Bhattacharya et al., 2015).

2 Extra results of application to pancreatic cancer dataset

At each quantile level, we examined the trace plots and autocorrelation plots of the posterior samples for various model parameters, which suggest good mixing of MCMC chains. Figure S1 and Figure S2 display the trace plots of the MCMC samples respectively for $B_2^\tau(t_l)$ and $\sigma^\tau(t_l)$ ($\tau = 0.1, 0.25, 0.5, 0.75, 0.9$), at 16 spectral locations indexed by the evenly spaced vector $l = 100, 200, \dots, 1600$. We also conducted Geweke tests to perform a formal convergence check on model parameters. Figure S3 demonstrates the distributions of the p-values from Geweke tests on $B_2^\tau(t_l)$ and $\sigma^\tau(t_l)$ for all the location indices $l = 1, 2, \dots, 1659$, which do not suggest a violation of the null distribution $Unif(0, 1)$ in each case. The proportions of p-values that are smaller than 0.05 are 0.058, 0.058, 0.061, 0.053, 0.059 respectively for $\tau = 0.1, 0.25, 0.5, 0.75, 0.9$.

The mean estimates of $B_2^\tau(t)$ ($\tau = 0.1, 0.25, 0.5, 0.75, 0.9$) and the corresponding 95% pointwise and simultaneous bands calculated from each approach are provided in Figure S4. A spectral location is flagged as significant if its SimBaS is less than or equal to 0.05 and its posterior estimate is greater than $\frac{1}{2} \log_2(1.5)$ in magnitude (corresponding to at least a 1.5-fold change and indicated by two horizontal lines in Figure S4), and is marked by a vertical line on the x-axis in the corresponding plot. For each approach, the mean estimate of $B_2^\tau(t)$ and identified locations differ greatly across quantiles. At $\tau = 0.1, 0.25, 0.5$, none of the approaches identify any location as significant; at $\tau = 0.75, 0.9$, certain locations are flagged by at least one approach. These comparisons across quantiles suggest that functional mean regression assuming a Gaussian distribution for the expression levels of a given protein within the same group could miss out on important proteomic differences between the cancer and normal cohorts, and functional quantile regression is strongly warranted in this case.

Comparing across methods at a given quantile, the two naïve approaches produce very wiggly estimate of $B_2^\tau(t)$, while the two-step bootstrap-based approaches appear to over-smooth the separate peaks in $B_2^\tau(t)$ that are recognized by the Bayesian FQR model into one single broader peak. The Bayesian FQR model consistently produces substantially tighter 95% simultaneous band than the alternatives, among which the naïve bootstrap-based QR always results in the widest simultaneous band. At $\tau = 0.75, 0.9$, the naïve Bayesian QR and our proposed model flag essentially the same set of spectral locations as significantly different between the cancer and normal populations; the two-step bootstrap-based methods are able to identify most of these locations and the naïve bootstrap-based QR nearly miss all of them.

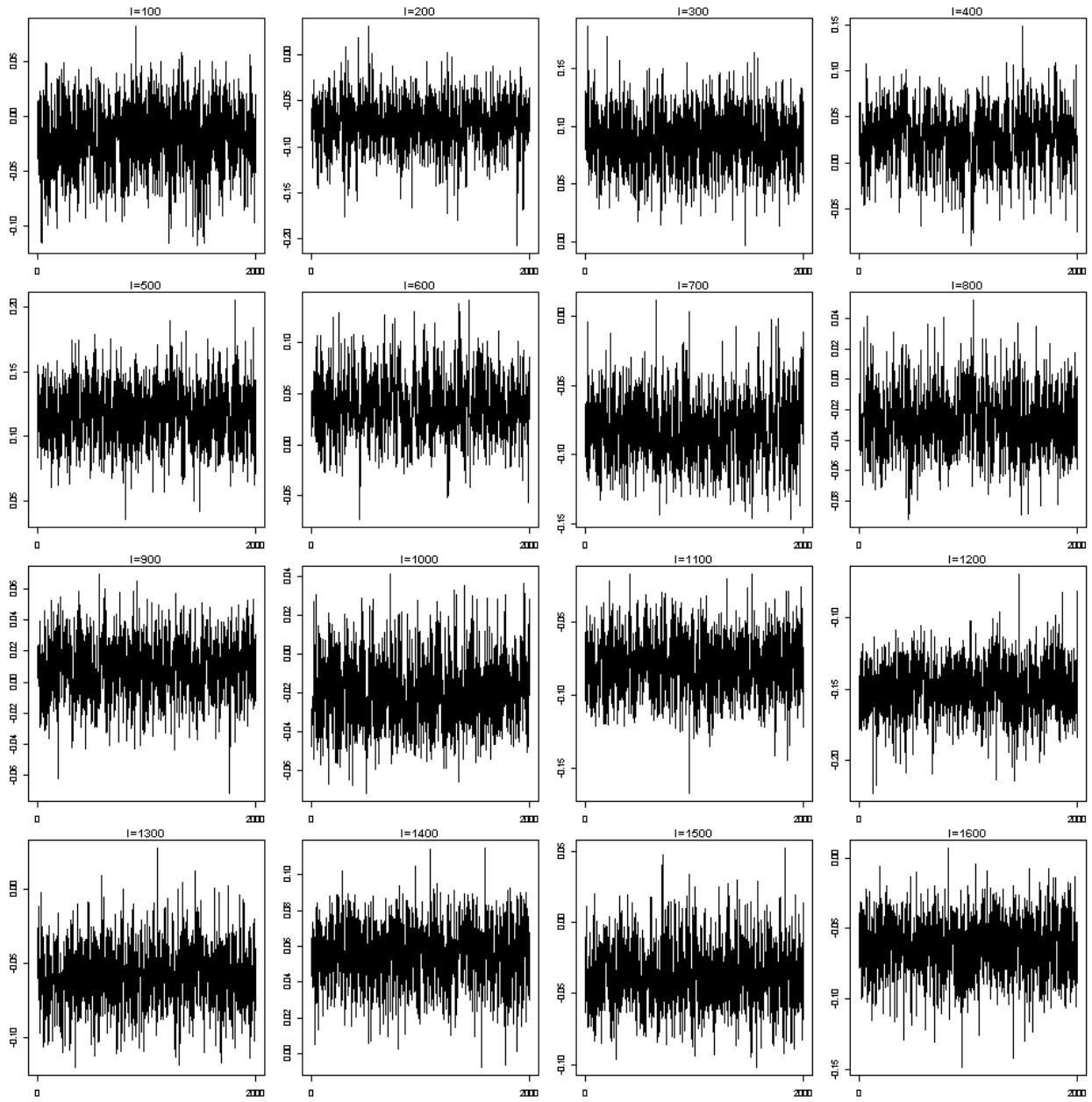


Figure S1(a): Trace plots of $B_2^{0.1}(t_l)$ in the pancreatic cancer dataset for a chosen subset of location indices l .

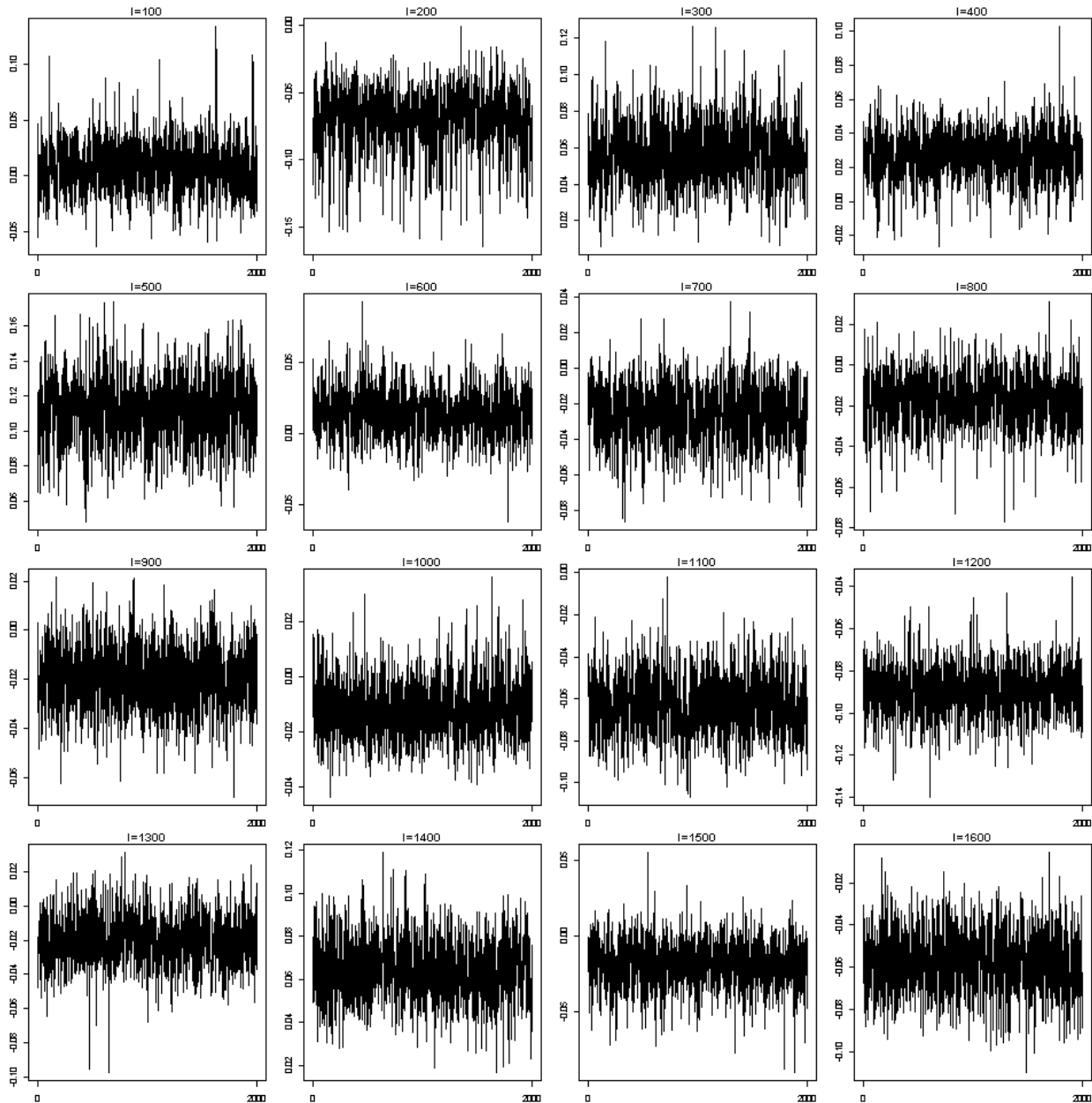


Figure S1(b): Trace plots of $B_2^{0.25}(t_l)$ in the pancreatic cancer dataset for a chosen subset of location indices l .

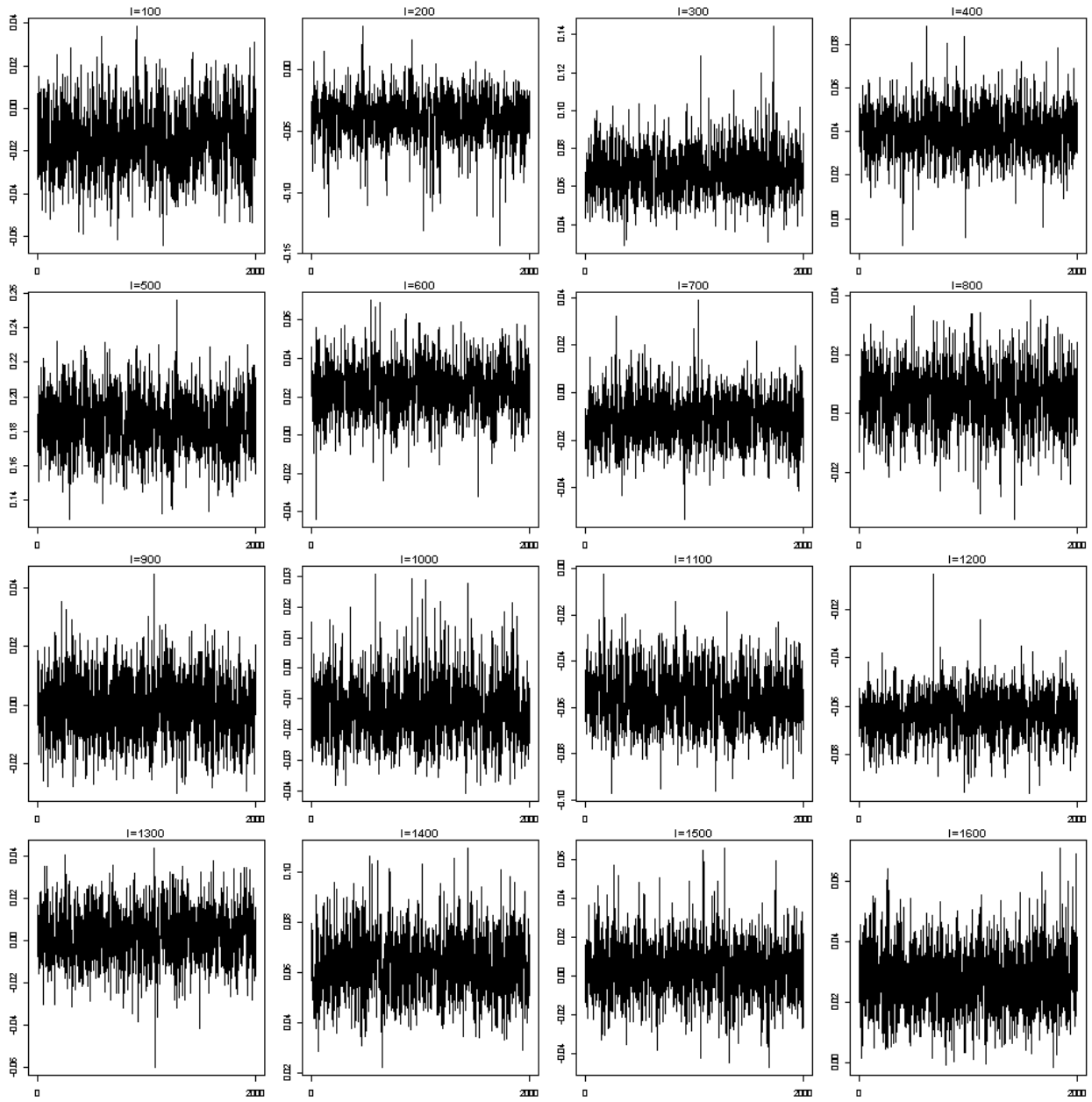


Figure S1(c): Trace plots of $B_2^{0.5}(t)$ in the pancreatic cancer dataset for a chosen subset of location indices l .

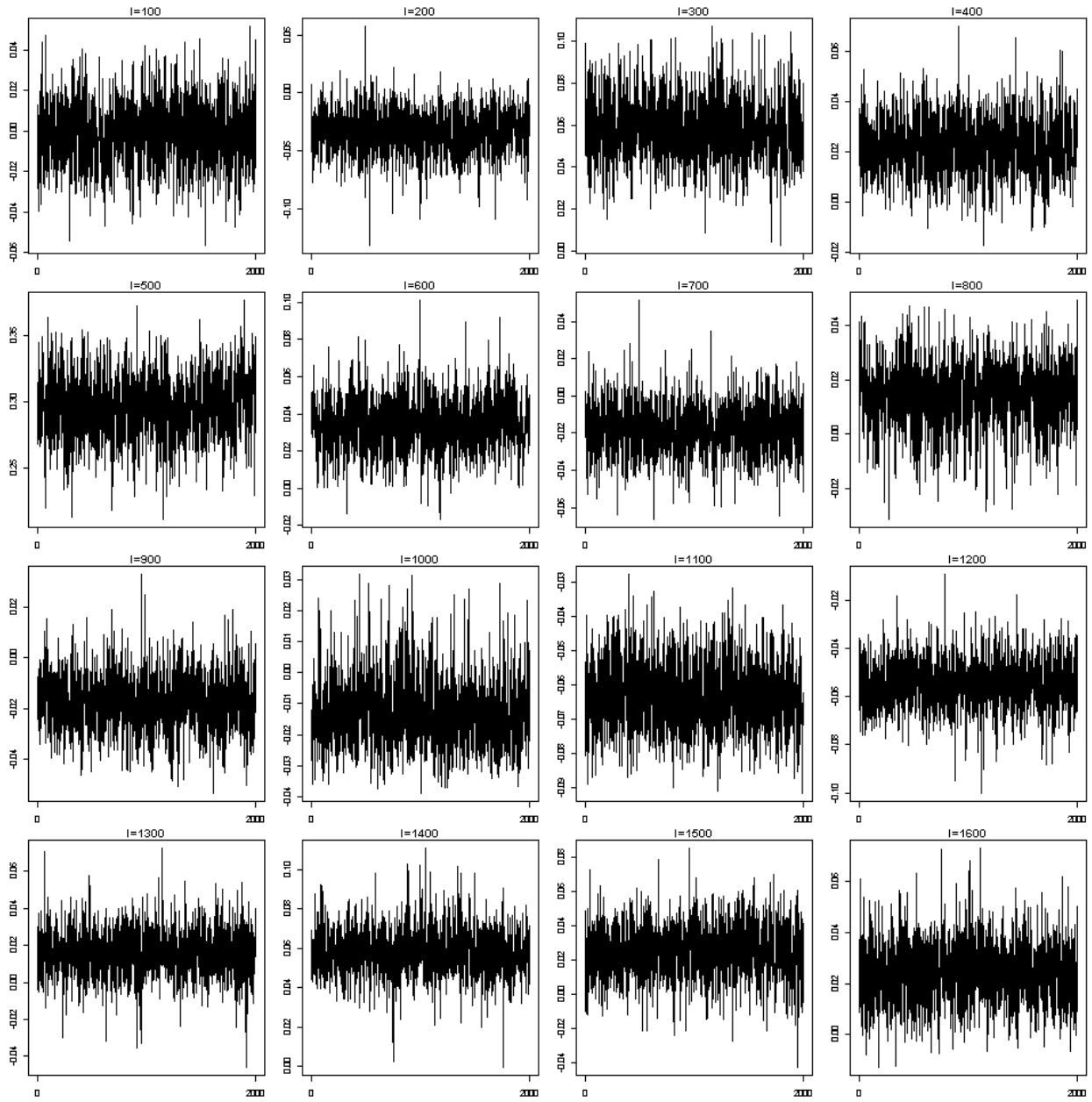


Figure S1(d): Trace plots of $B_2^{0.75}(t_l)$ in the pancreatic cancer dataset for a chosen subset of location indices l .

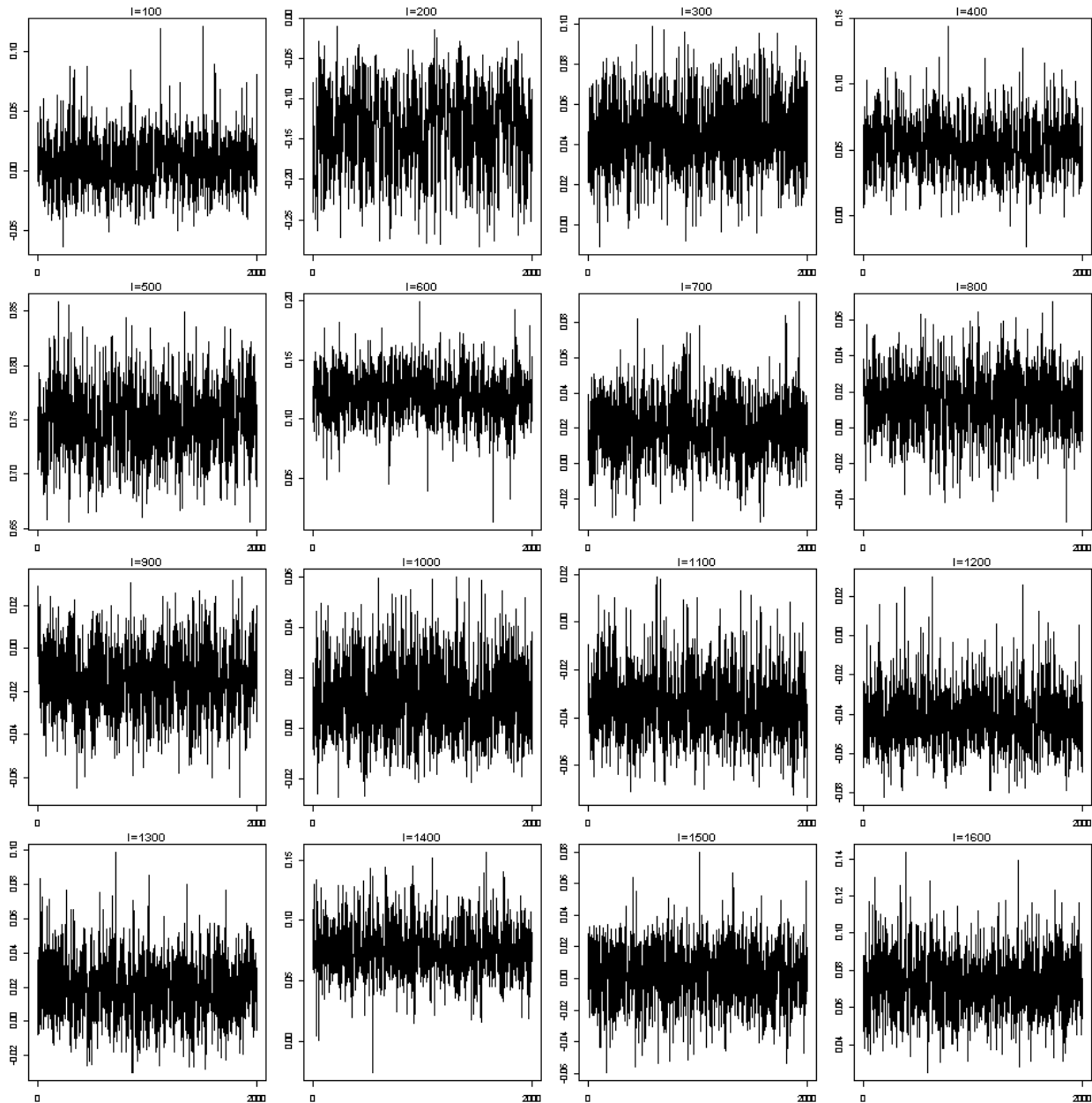


Figure S1(e): Trace plots of $B_2^{0.9}(t)$ in the pancreatic cancer dataset for a chosen subset of location indices l .

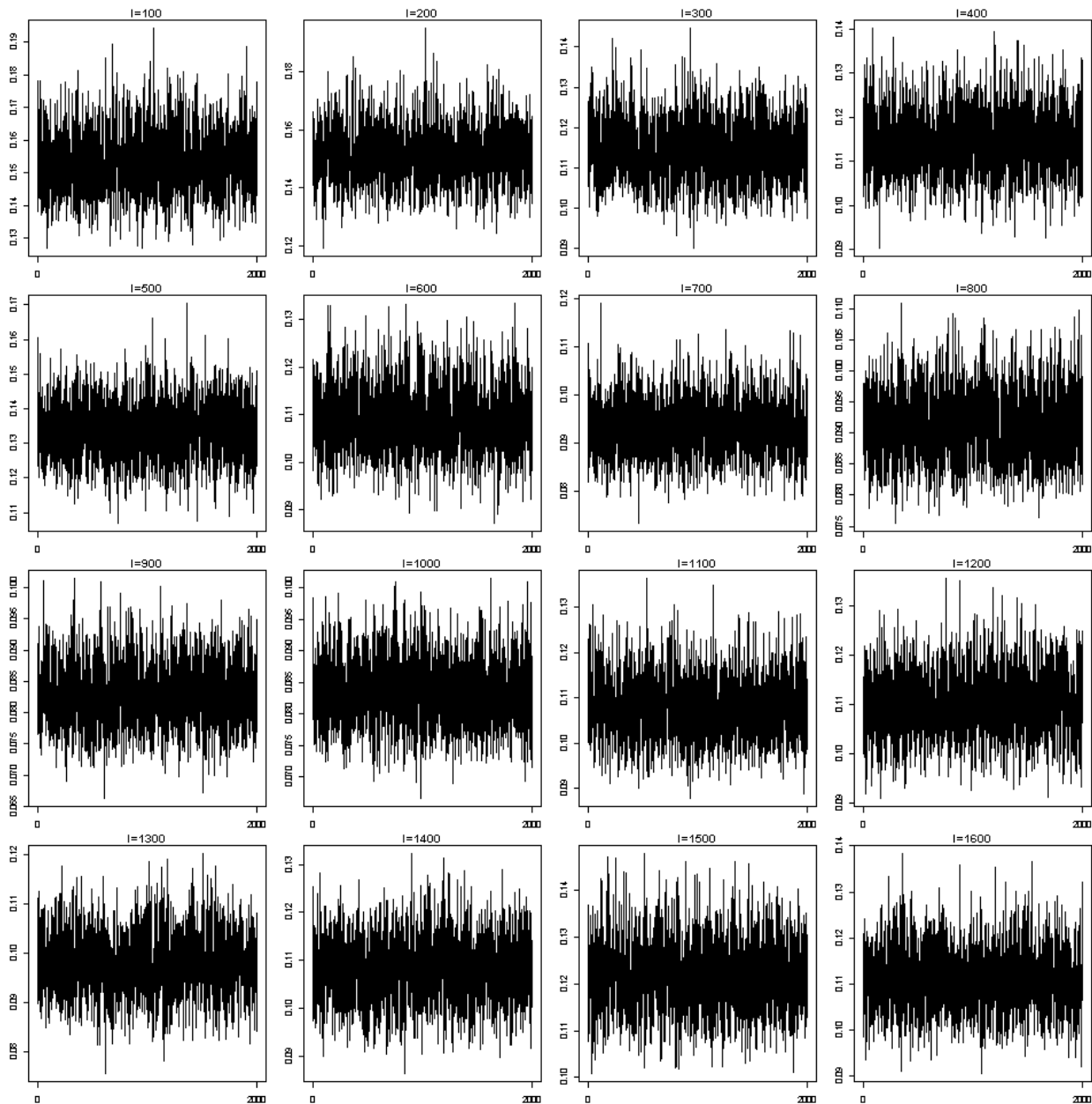


Figure S2(a): Trace plots of $\sigma^{0.1}(t_l)$ in the pancreatic cancer dataset for a chosen subset of location indices l .

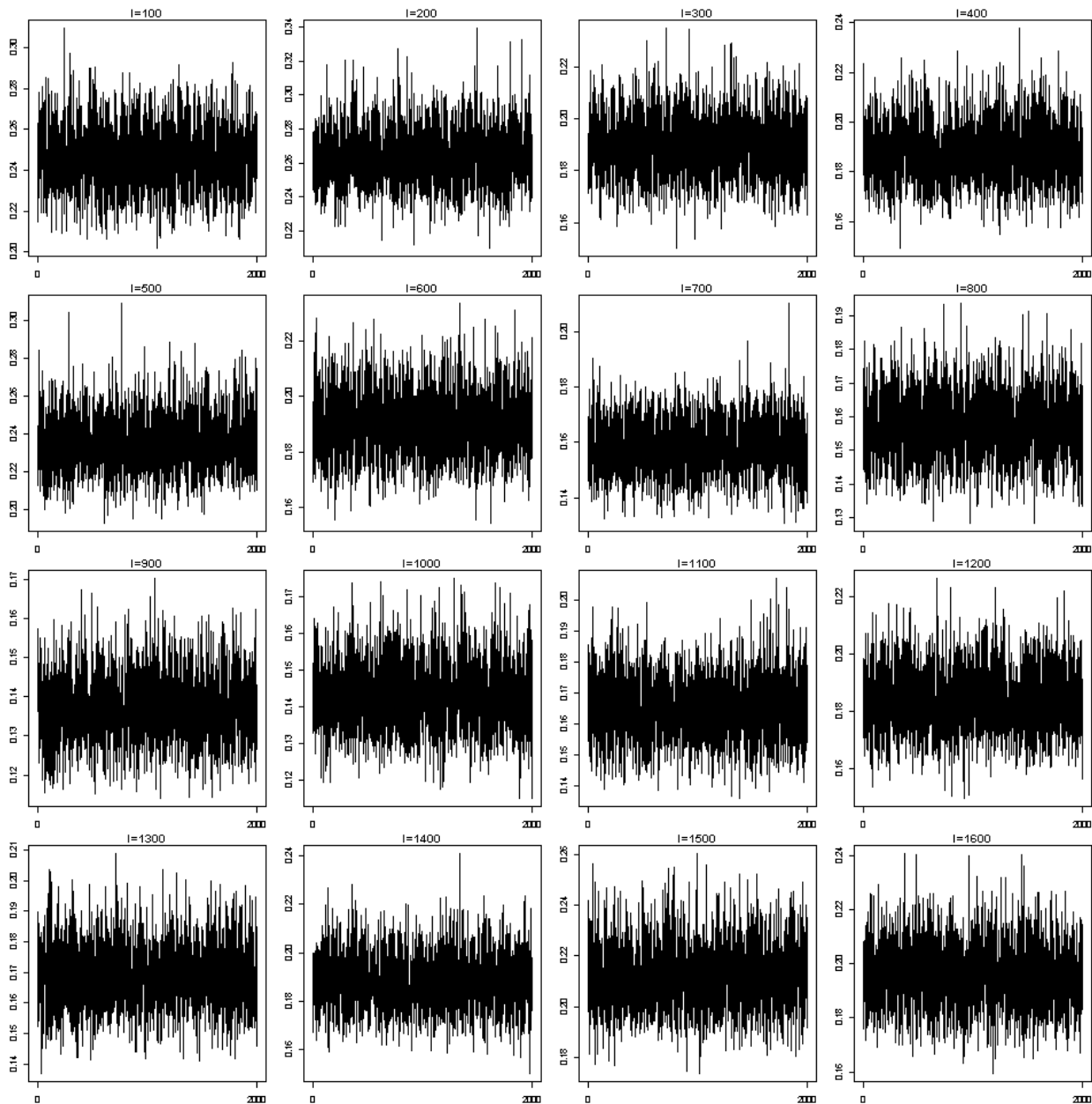


Figure S2(b): Trace plots of $\sigma^{0.25}(t_l)$ in the pancreatic cancer dataset for a chosen subset of location indices l .

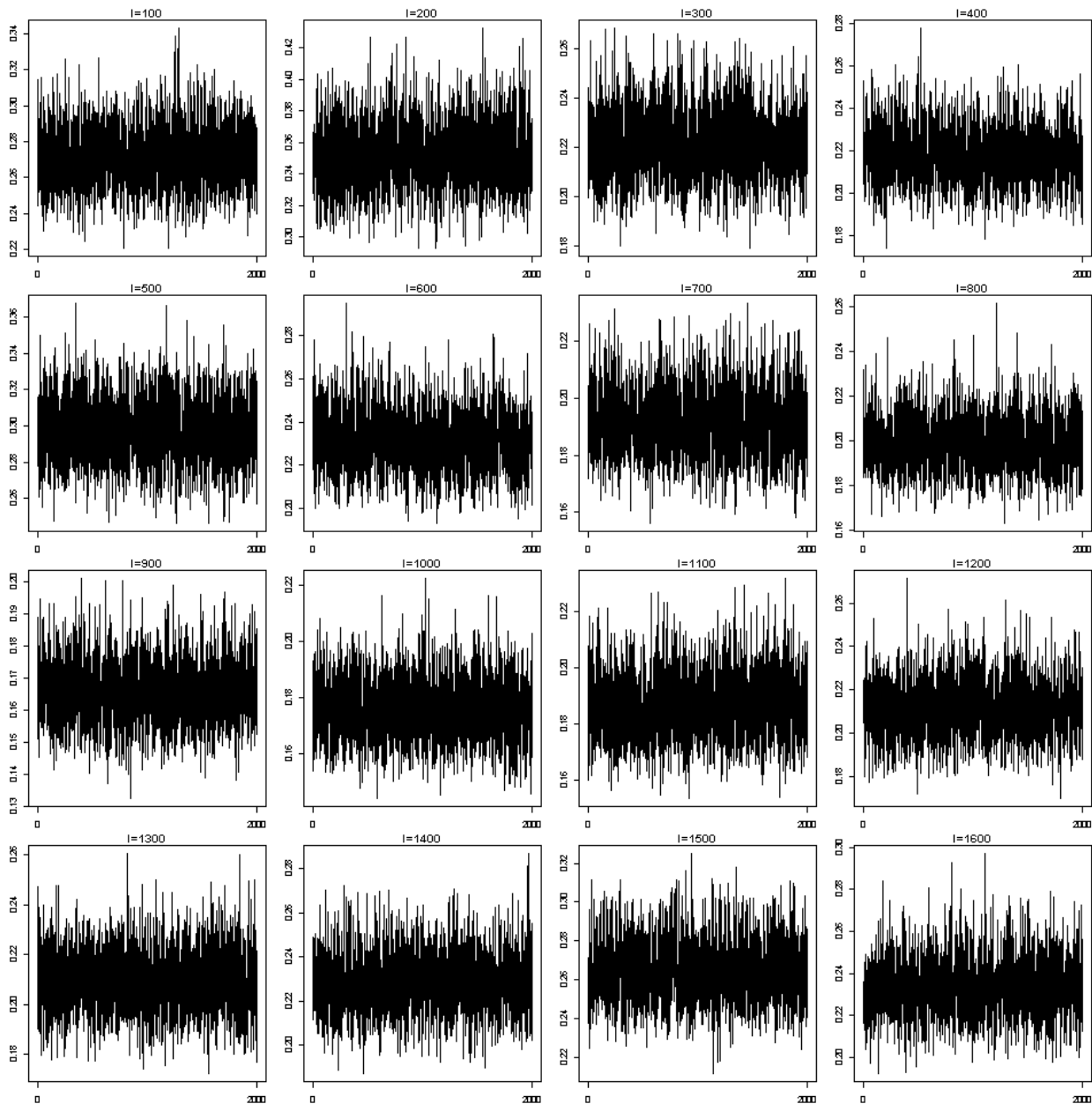


Figure S2(c): Trace plots of $\sigma^{0.5}(t_l)$ in the pancreatic cancer dataset for a chosen subset of location indices l .

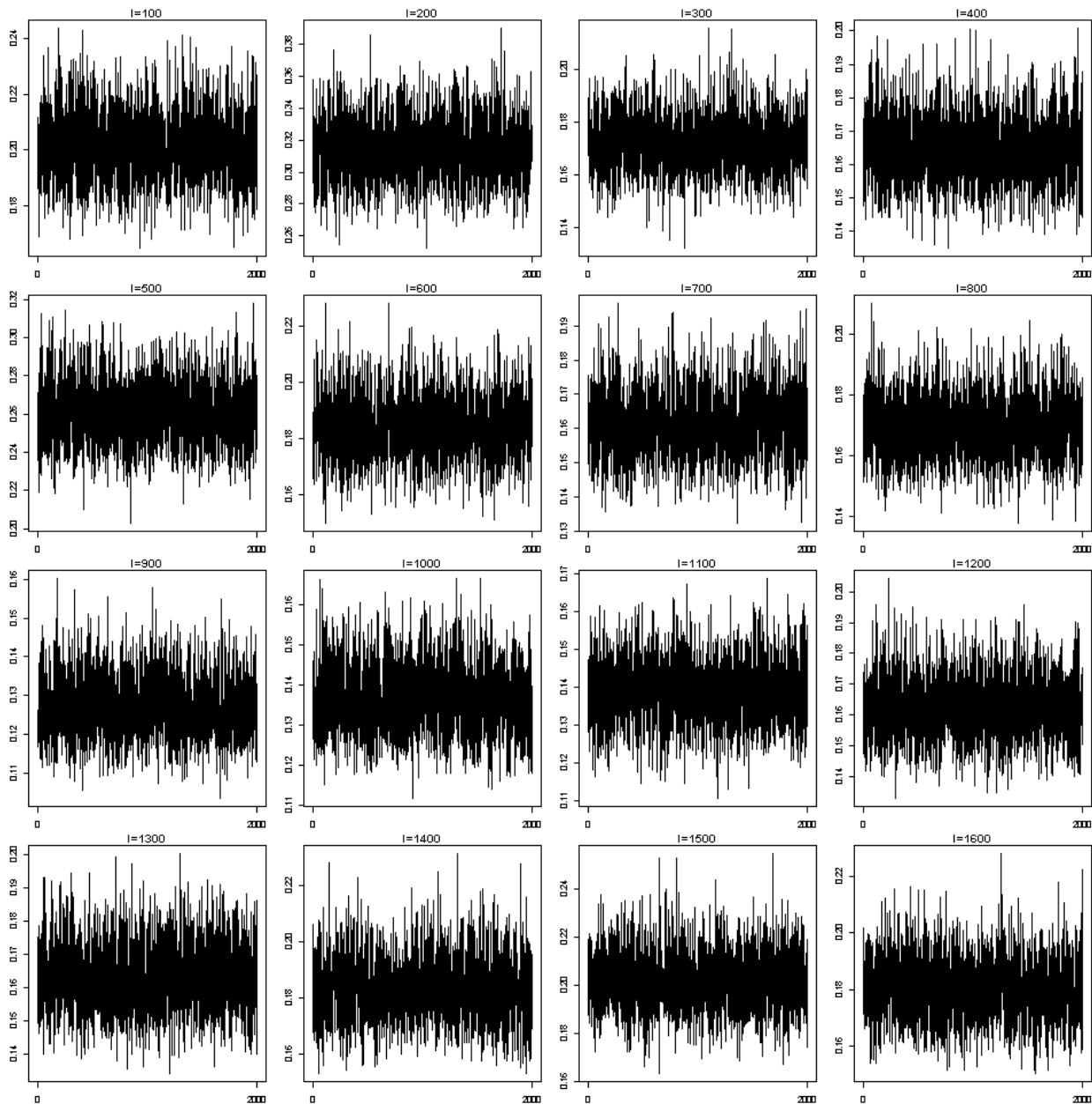


Figure S2(d): Trace plots of $\sigma^{0.75}(t_l)$ in the pancreatic cancer dataset for a chosen subset of location indices l .

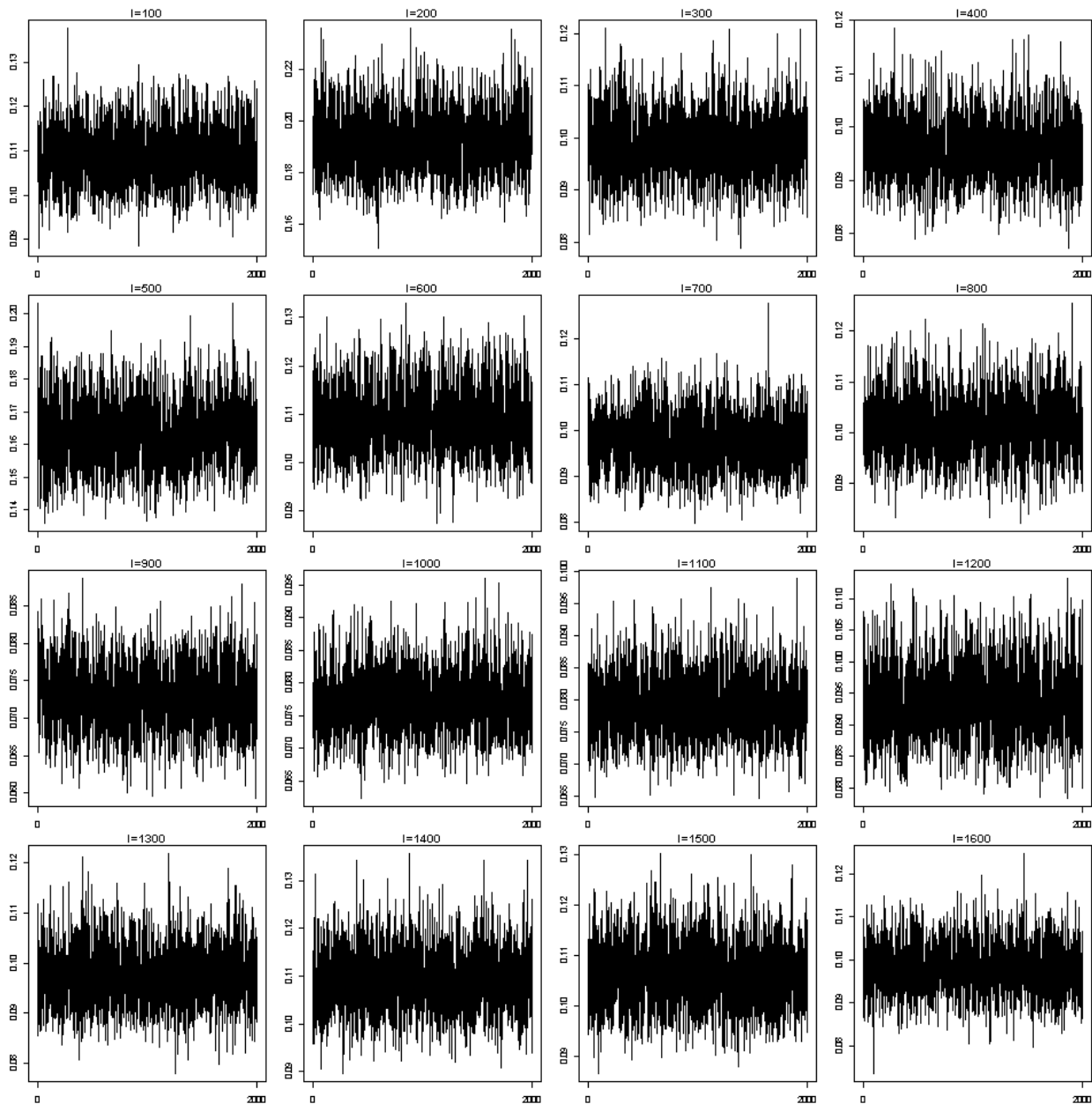


Figure S2(e): Trace plots of $\sigma^{0.9}(t_l)$ in the pancreatic cancer dataset for a chosen subset of location indices l .

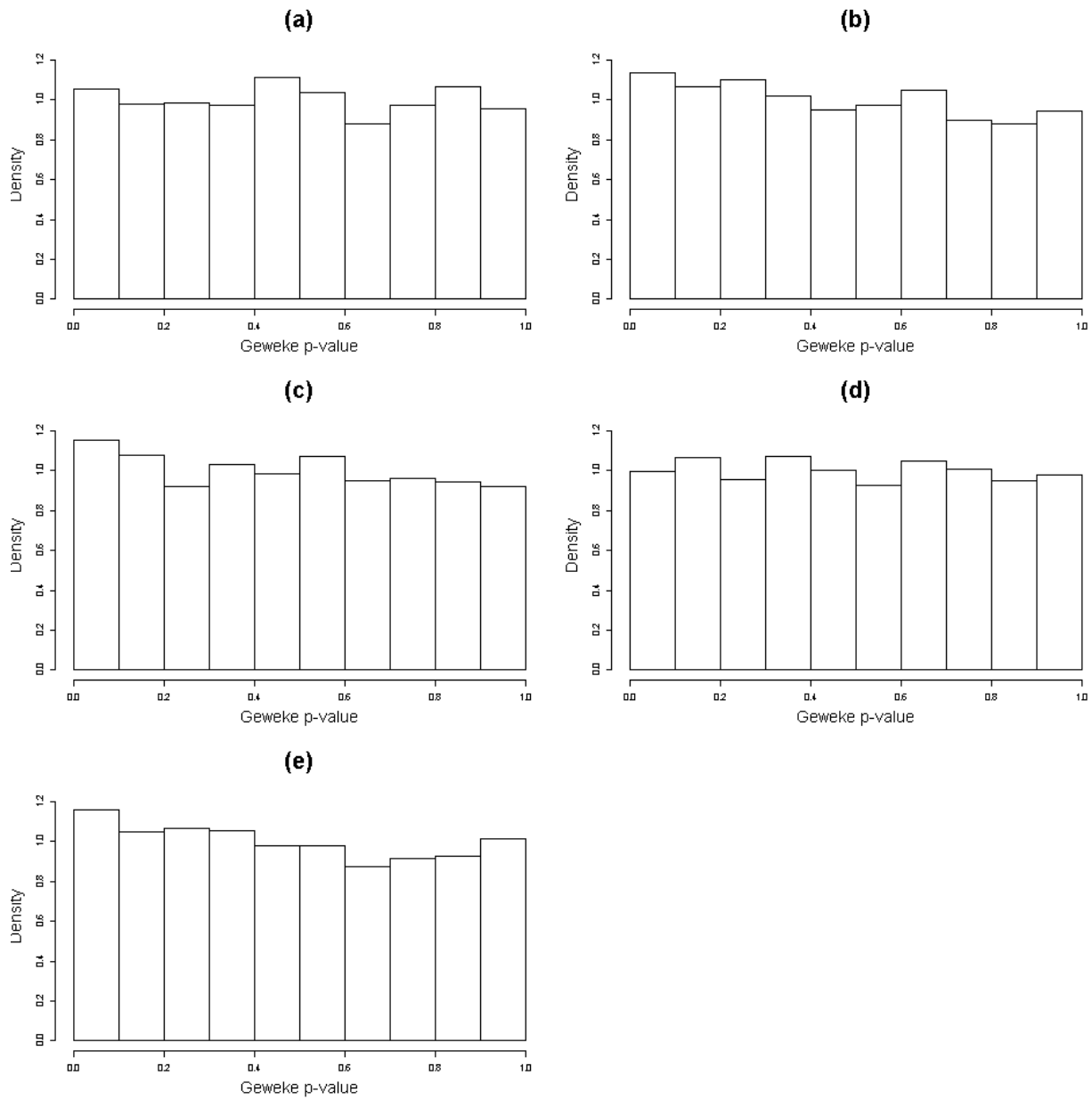


Figure S3: Distribution of p-values from Geweke tests on $B_2^{\tau}(t_l)$ and $\sigma^{\tau}(t_l)$ for all location indices l in the pancreatic cancer dataset, respectively for (a) $\tau = 0.1$, (b) $\tau = 0.25$, (c) $\tau = 0.5$, (d) $\tau = 0.75$, (e) $\tau = 0.9$.

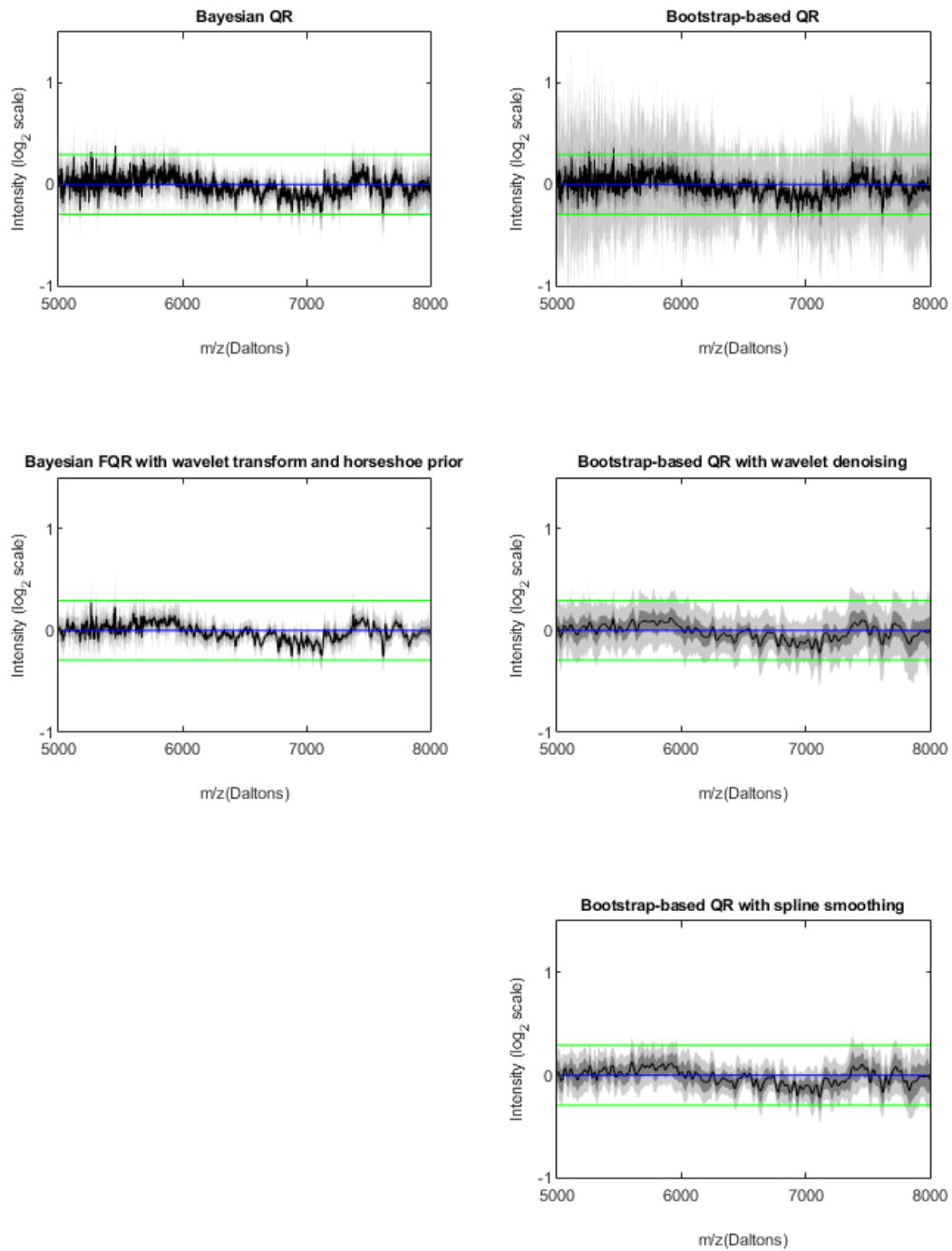


Figure S4(a): Cancer main effect function $B_2^{0.1}(t)$ in the pancreatic cancer dataset estimated by various methods, with 95% pointwise and simultaneous credible bands.

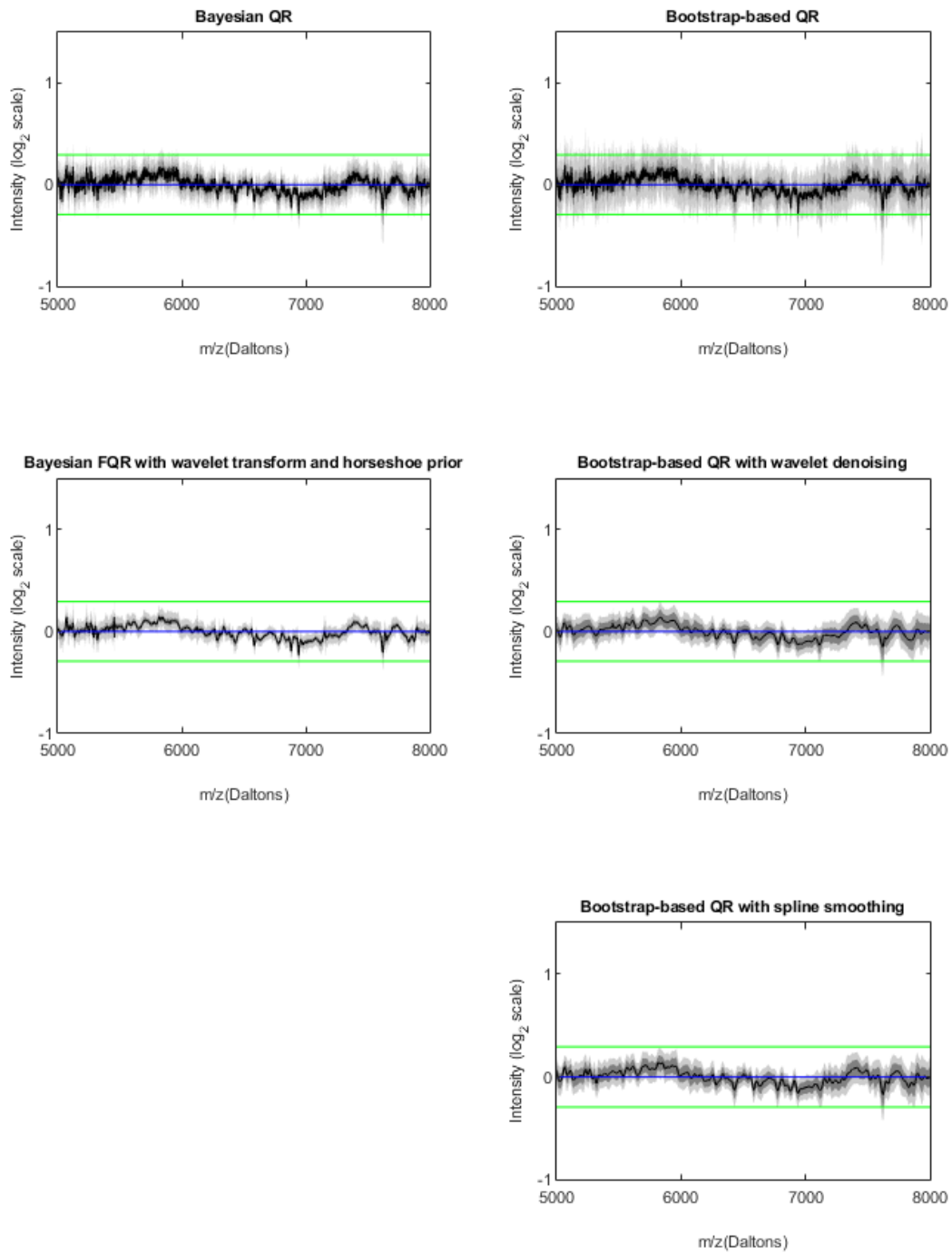


Figure S4(b): Cancer main effect function $B_2^{0.25}(t)$ in the pancreatic cancer dataset estimated by various methods, with 95% pointwise and simultaneous credible bands.

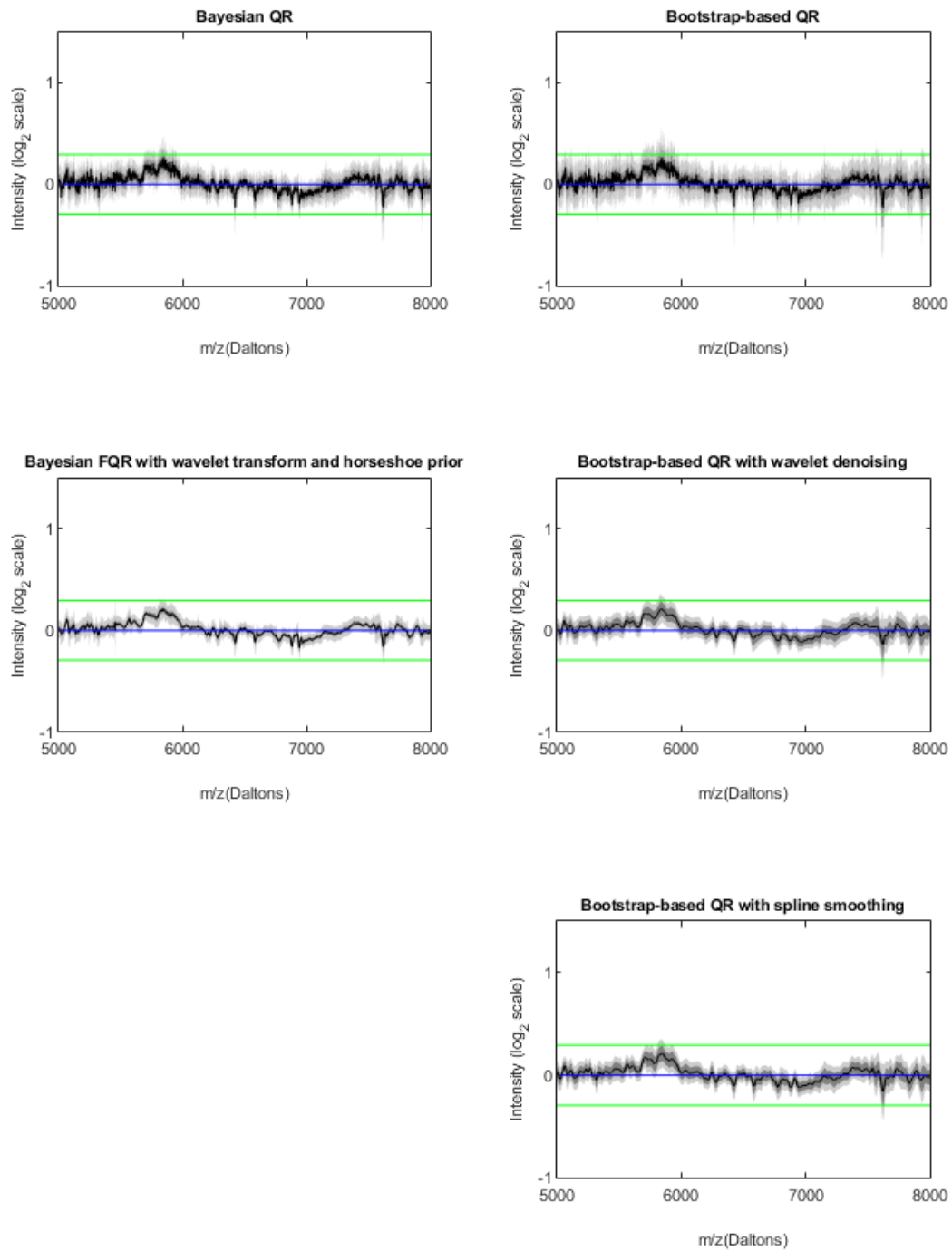


Figure S4(c): Cancer main effect function $B_2^{0.5}(t)$ in the pancreatic cancer dataset estimated by various methods, with 95% pointwise and simultaneous credible bands.

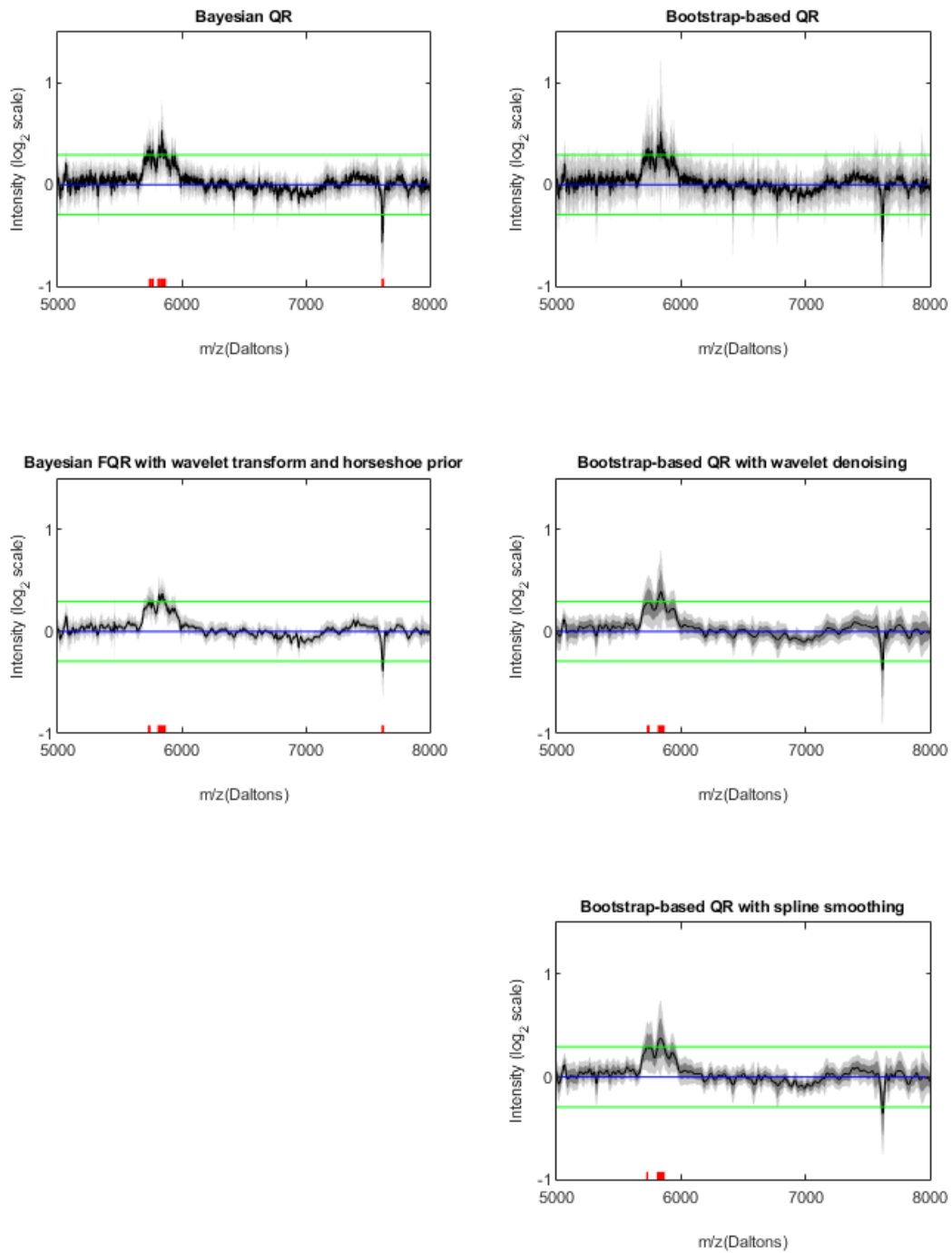


Figure S4(d): Cancer main effect function $B_2^{0.75}(t)$ in the pancreatic cancer dataset estimated by various methods, with 95% pointwise and simultaneous credible bands. Spectral locations that are flagged as significant are marked on the x-axis.

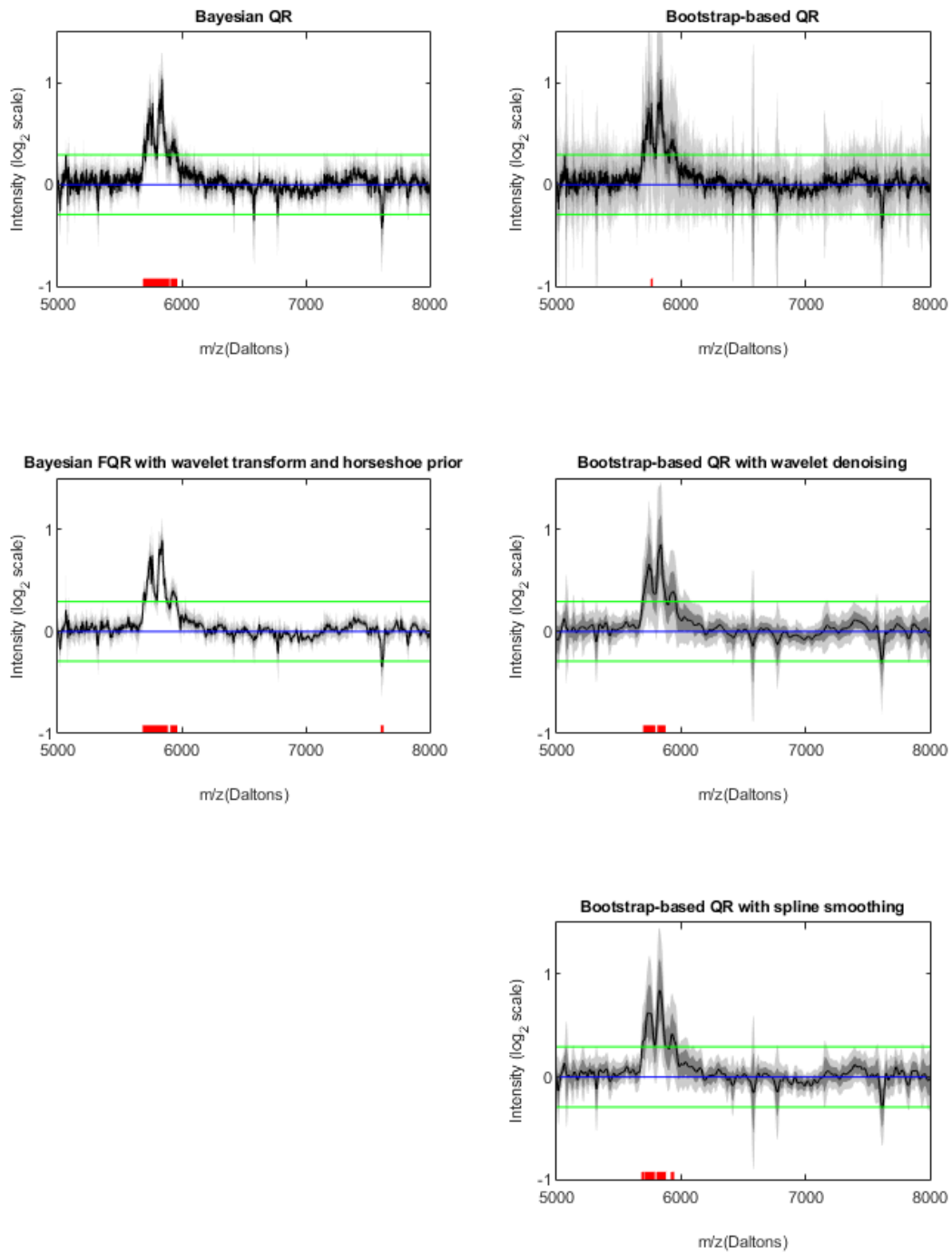


Figure S4(e): Cancer main effect function $B_2^{0.9}(t)$ in the pancreatic cancer dataset estimated by various methods, with 95% pointwise and simultaneous credible bands. Spectral locations that are flagged as significant are marked on the x-axis.

3 Implementation details of FDboost package

We called the R package "FDboost" (Brockhaus and Ruegamer, 2017) to apply the boosting functional regression model proposed by (Brockhaus et al., 2015) to 10 replicate simulation datasets in the right skewed setting to perform FQR for $\tau = 0.9$.

A linear base learner with $df = 1$ was specified for the group effect covariate, and a smooth P-spline base learner with $df = 20$ was specified for the non-linear effect in t direction. A composed basis was constructed by combining these two base learners using the $\%A0\%$ operator, so that only the marginal basis in t direction was regularized by a L2 penalty. Model estimation was performed by component-wise gradient boosting. As recommended by the authors, we determined the optimal number of boosting iterations from a search grid of 1 to 2000 by cross validation while fixing the step-length $\nu = 0.2$. For each replicate dataset, we found that the point estimate of the group main effect function $B_2^{0.9}(t)$ based on the model fit corresponding to the optimal number of boosting iterations was identically 0, and this process took 10 minutes on a 64-bit operating system with 2 processors and an RAM of 256GB.

We then repeated the model fitting and tuning process above with different specifications, which are manually chosen to be more appropriate for spiky and spatially heterogeneous functional data. Specifically, we used 150 knots, 1st order regression spline, and ridge penalty for the base learner modeling non-linear effect in t direction. This time we were able to get a reasonable but very noisy point estimate of $B_2^{0.9}(t)$.

References

- Bhattacharya, A., D. Pati, N. S. Pillai, and D. B. Dunson (2015). Dirichlet–laplace priors for optimal shrinkage. *Journal of the American Statistical Association* 110(512), 1479–1490.
- Brockhaus, S. and D. Ruegamer (2017). *FDboost: Boosting Functional Regression Models*.
- Brockhaus, S., F. Scheipl, T. Hothorn, and S. Greven (2015). The functional linear array model. *Statistical Modelling* 15(3), 279–300.

- Carvalho, C. M., N. G. Polson, and J. G. Scott (2009). Handling sparsity via the horseshoe. In *Artificial Intelligence and Statistics*, pp. 73–80.
- Griffin, J. E., P. J. Brown, et al. (2010). Inference with normal-gamma prior distributions in regression problems. *Bayesian Analysis* 5(1), 171–188.
- Makalic, E. and D. F. Schmidt (2016). A simple sampler for the horseshoe estimator. *IEEE Signal Processing Letters* 23(1), 179–182.